InP Quantum Dot based Light-emitting and Neuro-stimulating Optoelectronic Devices

by
Onuralp Karatüm

A Thesis Submitted to the
Graduate School of Sciences and Engineering
in Partial Fulfillment of the Requirements for
the Degree of

Master of Science
in
Electrical and Electronics Engineering

Koc University

August 2019

Koc University

Graduate School of Sciences and Engineering

This is to certify that I have examined this copy of a master's thesis

by
Onuralp Karatüm

and have found that it is complete and satisfactory in all respects,
and that any and all revisions required by the final
examining committee have been made.

Committee Members:

_____
Asst. Prof. Sedat Nizamoğlu (advisor)

_____
Prof. Alphan Sennaroğlu

_____
Asst. Prof. Onur Ferhanoğlu

Date: _____

Dedicated to

my mother Emine Karatüm,

my father Mustafa Karatüm,

and my brother Osman Karatüm

I love you more than anything.

ABSTRACT

The discovery of semiconductor nanocrystals, also called as quantum dots (QDs), has led to remarkable research both on the understanding the fundamentals of these nanocrystals and on their applications to vast number of optoelectronic devices. QD based light-emitting devices (QLEDs), lasers, and solar cells are a few examples of semiconductor nanocrystal based optoelectronic devices. This interest to QDs stems from their outstanding optical and structural properties such as tunable band gap, high quantum efficiency, solution processability, emission and absorption in visible spectrum and nanoscale size.

This thesis demonstrates two different optoelectronic device technologies, LEDs and neural stimulation electrodes, that use indium phosphide (InP) based QDs as active layer material.

Most of the existing QLED studies were conducted with cadmium (Cd) containing QDs, which poses a problem for their commercialization due to their toxicity. Here, we show a newly synthesized alternative material, InP QDs covered with zinc oxide (ZnO) shell, and its application to QLEDs. We present the QLED design by proper choice of materials, fabrication of solution processed QLEDs, characterization of QD nanostructure via adjusting the shell thickness, and optimization of layer thicknesses for maximizing efficiency parameters.

As the second part of the thesis, we present InP QD based photoelectrodes for the stimulation of neurons via light. We illustrate the design of InP QD based photoelectrodes that can produce both cathodic and anodic photocurrent, which can both stimulate and silence neurons. We discuss the photoelectrical performances of core and core/shell QD based photoelectrodes. After the optimization of device layers and QD nanostructure, we present the electrophysiology experiments which show the membrane potential variations of neurons under illumination that are grown on our photoelectrodes.

By integrating QDs into convenient device architectures, InP QDs can be used for efficient LEDs and effective neural stimulation electrodes. Characterization and optimization of QD nanostructure and device structure is crucial for producing efficient and effective optoelectronic devices with QDs.

ÖZET

Yarıiletken nanokristallerin, diğer adıyla kuantum noktalarının (QD) keşfi hem bu nanokristallerin temel prensiplerini anlamak yolunda, hem de bunların birçok farklı optoelektronik aygıta uygulaması konusunda çok fazla araştırmaya yol açmıştır. QD tabanlı ışık yayan aygıtlar (QLED), lazerler ve güneş pilleri yarıiletken nanokristal tabanlı optoelektronik aygıtlardan birkaçıdır. QD'lere olan bu ilgi, bu nanokristallerin ayarlanabilir bant aralığı, yüksek kuantum verimliliği, çözeltiden işlenebilirliği, görünür spektrumda ışıma ve soğurma yapabilmeleri ve nanometrik boyutlarda olmaları gibi seçkin optik ve yapısal özelliklerinden kaynaklanmaktadır.

Bu tezde indiyum fosfat (InP) tabanlı QD'leri aktif tabaka malzemesi olarak kullanan iki farklı optoelektronik aygıt teknolojisi, LED ve sinir uyarım elektrotları, gösterilecektir.

Mevcut QLED çalışmalarının çoğu kadmiyum (Cd) içeren QD'ler ile yapılmıştır. Bu da Cd'nin zehirliliği sebebiyle QLED'lerin ticarileştirilmelerinin önünde bir problem oluşturmaktadır. Biz bu tezde yeni sentezlenen alternatif bir materyali, çinko oksit (ZnO) kabuğuyla kaplanmış InP QD ve bunların QLED'lere uygulamasını göstereceğiz. Uygun materyallerin seçimi ile QLED tasarımını, çözeltiden işlenmiş QLED'lerin fabrikasyonunu, kabuk kalınlığının ayarlanması yoluyla QD nano yapısının karakterizasyonunu ve verimlilik parametrelerinin maksimizasyonu için tabaka kalınlıklarının optimizasyonunu göstereceğiz.

Tezin ikinci kısmı olarak, InP QD tabanlı fotoelektrotların sinirlerin ışık ile uyarılması amacı ile kullanımını göstereceğiz. Hem katodik hem de anodik fotoakım üreterek nöronları hem uyarabilen hem de susturabilen InP QD tabanlı fotoelektrotların tasarımından bahsedeceğiz. Çekirdek ve çekirdek/kabuk tabanlı aygıtların fotoelektrik performanslarını tartışacağız. Aygıt tabakalarının ve QD nano yapısının optimizasyonundan sonra, elektro fizyoloji deneyleri ile fotoelektrotlarımız üzerinde büyütülen nöronların ışık altında hücre zarı potansiyellerindeki değişimleri göstereceğiz.

QD'lerin uygun aygıt mimarilerine entegre edilmesiyle, InP tabanlı QD'ler verimli LED'ler ve etkili sinir uyarım fotoelektrotları için kullanılabilir. QD nano yapısının ve aygıt yapısının karakterizasyonu ve optimizasyonu, verimli ve efektif QD tabanlı optoelektronik aygıtların üretilebilmesi için çok kritiktir.

ACKNOWLEDGEMENTS

I am greatly indebted to my advisor Dr. Sedat Nizamoğlu for giving me the opportunity to work with him. His encouragement, support and guidance always motivated me to do my best, while his positive personality created an enjoyable working environment.

I thank my committee members, Dr. Alphan Sennaroğlu and Dr. Onur Ferhanoğlu, for their valuable feedbacks and comments about my work.

I owe many thanks to all the members of IDEALAB for their contribution to my work, fruitful discussions, and also for the fun and warm environment they created in the office, laboratory and out of work.

My girlfriend Rüya makes me happier and more joyful each day. I thank her a lot.

Lastly, endless thanks to my mother Emine, my father Mustafa, and my brother Osman for their unconditional love and support. I cannot thank them enough. I feel so lucky to have them.

I acknowledge the financial support of the Scientific and Technological Research Council of Turkey (TÜBİTAK) (2210 National Scholarship Programme for MSc students, Project Nos. 115E242 and 115E115), and European Research Council (ERC) under the European Union's Horizon 2020 Research and Innovation Programme (639846).

TABLE OF CONTENTS

LIST OF FIGURES

LIST OF TABLES

CHAPTER 1 Introduction

The conversion between electricity and light forms the basis of numerous technologies we encounter in everyday life. Light-emitting devices (LEDs) used in cell phones, televisions, traffic lights, and in many other technologies are examples of tools that perform conversion of electricity into light. Photodiodes used in cameras, and solar cells as today's and future's "green" energy harvesters are devices that operate by converting light into electricity. Our eyes are equipped with photoreceptors, which are the cells that convert optical signals into meaningful electrical signals that are sent to the brain for the formation of vision.

The electricity to light or light to electricity transducers are called "optoelectronic devices". With the continuously broadening understanding of the behavior of electrons and light, people have developed numerous high-level optoelectronic technologies (organic LEDs, ultrafast lasers, high resolution cameras, low-loss optical fibers, etc.) and continue to do so. However, rapid growth of optoelectronic technologies and industry brings the problem of electronic waste (e-waste). According to the *Global E-waste Monitor 2017*, nearly 45 million of metric tons of e-waste was generated world-wide, and 80% of it was not recycled properly (1, 2). This raises major concerns about environmental sustainability. It also affects many people's health adversely due to the inappropriate collection of e-waste in informal recycling sites (3). Electronic devices contain different toxic materials such as mercury (Hg), lead (Pb), cadmium (Cd) which are known to have neurotoxic effects on humans (4). Today, one of the priorities of research studies and industrial works is to discover alternative non-toxic materials to eliminate the toxicity of electronic devices.

Following their discovery in 1980s by Alexey I. Ekimov and Louis Brus (5, 6), semiconductor nanocrystals, also known as quantum dots (QDs), created a whole new research field branching into QD chemistry, QD physics, QD applications into electronics, optics, biology and many more. However, the most studied QDs contain toxic materials such as Cd, and Pb, which urges researchers to explore alternative materials for the synthesis of non-toxic QDs. Indium phosphide (InP) QDs are one of the widely studied QDs that are considered as an alternative to their toxic counterparts, and also are reported to be non-toxic (7, 8).

This thesis demonstrates the application of InP-based QDs to two different optoelectronic technologies: *i) light-emitting devices (LEDs), ii) neural stimulation electrodes.* The organization of the thesis is as follows:

In the first chapter, we make a general introduction to the topics of optoelectronics and QDs.

In the second chapter, we provide basic background knowledge of the electronic, optical and structural properties of colloidal quantum dots; working mechanism, fabrication and performance metrics of QLEDs.

In the third chapter, we first make a brief introduction to our QLED study. Then, we explain the fabrication of our QLEDs, QD nanostructure optimization, device structure and band alignment of the constituent materials, and the performance of the optimized devices. We close the chapter with concluding remarks.

In the fourth chapter, we first explain neural stimulation and photoactive surfaces in the introduction section. Then, we demonstrate the photoelectrode fabrication, QD characterization, photoelectrode design, and finally present the experimental results.

In the fifth chapter, we close the thesis with general concluding points and discussions.

CHAPTER 2 Background

2.1 Colloidal Quantum Dots

Colloidal quantum dots, also known as semiconductor nanocrystals, are nano-sized crystals that are composed of semiconducting materials. Their diameter is generally in the range of 2-10 nanometer. Quantum dots have different structures such as core and core/shell, and different types such as type I and type II according to the energy alignment of core and shell.

2.1.1 Electronic Properties

One of the most intriguing properties of quantum dots is the ability to control their band gap by properly adjusting their size. This is a result of quantum confinement effect, which is a size-related phenomenon that leads to changes in the electrical and optical properties of a particle when the radius of the particle becomes smaller than the Bohr radius of the bulk material. It is known that a single atom has discrete energy levels that electrons and holes can occupy, while in bulk materials those energy levels become continuous. Regarding the electronic properties, quantum dots can be considered as intermediate state between an atom and a bulk material, because they have discrete energy levels, but they also consist of many numbers of atoms (mostly 1000 to 100000 atoms). Fig. 1 (9) visualizes the energetic structure of bulk and quantum dots with different sizes.

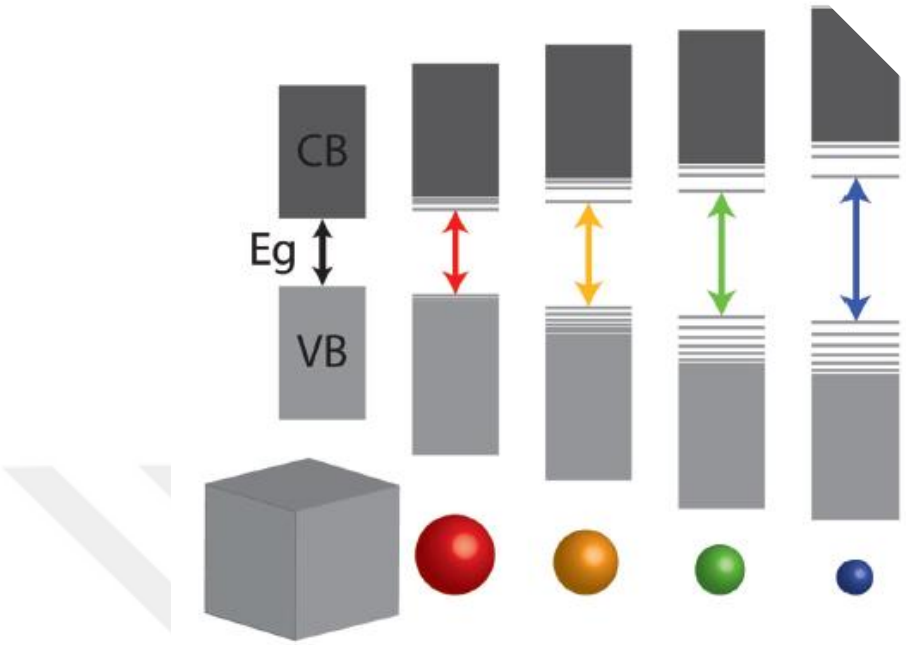

Figure 1: Electronic energy structure of quantum dots with different sizes, ranging from bulk to smaller sizes (9).

If we visualize quantum dots as a spherical volume of crystallite and consider the spatial confinement of electron and hole in that spherical volume, the band gap energy of quantum dots can be written in the following form (10)

$$E_g \cong E_{g,bulk} + \frac{h^2\pi^2}{2R^2}\left(\frac{1}{m_e^*} + \frac{1}{m_h^*}\right) - \frac{1.8e^2}{\epsilon R} \qquad (1)$$

where $E_{g,bulk}$ is the band gap of the bulk material, m_e^* and m_h^* are respectively electron and hole effective mass, and E_{Ry} is the Rydberg energy. Increasing the size of the quantum dot results in a smaller band gap, while decreasing the size provides a larger band gap. Ability of controlling the band gap gives rise to many advantageous optical properties that make the application of quantum dots in many optoelectronic devices feasible.

c

2.1.2 Optical Properties

Having a tunable band gap, the emission of quantum dots can be adjusted by properly controlling their size. The size of the quantum dots can be controlled during the synthesis. This way, the same

quantum dot can be made to emit in different regions of electromagnetic spectrum like blue, green and red. Fig. 2 (11) shows different sizes of CdSe nanocrystals from 2.3 nm to 5.5 nm, which have emission peak wavelengths changing from 470 nm to 620 nm.

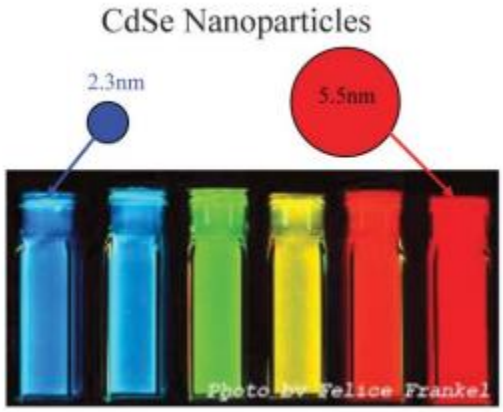

Figure 2: Different sizes of CdSe quantum dots emit in different colors. Changing size from 2.3 nm to 5.5 nm progressively corresponds to shifting of emission peak wavelength from 470 nm to 620 nm (11).

The highest wavelength that a quantum dot can emit depends on its bulk band gap. Since the band gap of the quantum dot cannot be made smaller than its bulk band gap, the emitted photon energy cannot be lower than the bulk band gap energy. For example, bulk band gap of CdSe is 1.7 eV (12), which means the highest wavelength that CdSe nanoparticles emit in theory is 730 nm from the following relation:

$$E = 1.7\ eV = \frac{hc}{\lambda} \implies \lambda \cong 730\ nm \qquad (2)$$

That means it is not possible to synthesize CdSe quantum dots which emit in infrared region (IR) of the electromagnetic spectrum. On the other hand, PbS has bulk band gap of 0.3 eV, which implies that the band gap of PbS quantum dots can be tuned to have emission in visible spectrum or IR.

Photoluminescence quantum yield (PL QY) is another important optical property that is considered especially for applications like quantum dot light-emitting devices (QLEDs) and quantum dot based luminescent solar concentrators. PL QY is defined as the ratio of number of emitted photons per number of absorbed photons. It is typically measured via an integrating sphere or relative to a dye of known PL QY. Covering QD core with a higher band gap shell material increases PL QY

by passivating the surface defect states of core. Many different types of materials have been used as shell in the literature such as ZnS, ZnSe, ZnO, ZnTe, CdS. The choice of shells mainly depends on the lattice mismatch between core material and shell material. The lower mismatch is preferable as it creates less strain between core and shell (13). Modern synthesis procedures has allowed PL QY values to exceed 95% (14). In a recent report, CdSe/CdS QDs with PL QY very close to unity (99.6 ± 0.2%) has been synthesized by Alivisatos et. al. (15). Achievement of such high PL QY merits make quantum dots suitable for applications in both electroluminescent and color-conversion QLEDs. Moreover, since reemission is an important process which affects the efficiency of luminescent solar concentrators, achieving PL QY close to unity might pave the way for the commercialization of solar concentrator technology.

Like emission, absorption of quantum dots can also be controlled by tuning the band gap as the absorbed photon must have an energy equal to at least the band gap. Quantum dots have high absorption coefficient (α) in visible and IR regions of the spectrum, at comparable levels with organic semiconductors. High absorption coefficient is a desirable property for applications such as solar cells and photodetectors as it decreases the absorption length (α^{-1}), which is the thickness required for absorbing the incident light. This enables fabrication of thinner devices (500 to 1000 nm) for solar cell and photodetection applications (16). As an example, Fig. 3 displays the absorption coefficient of bulk PbS and PbS quantum dots as a function of photon energy and wavelength (17). The absorption coefficient of PbS quantum dots is on the order of 10^5-10^6 cm^{-1} in visible spectrum, which results in α^{-1} values of several hundred nanometers.

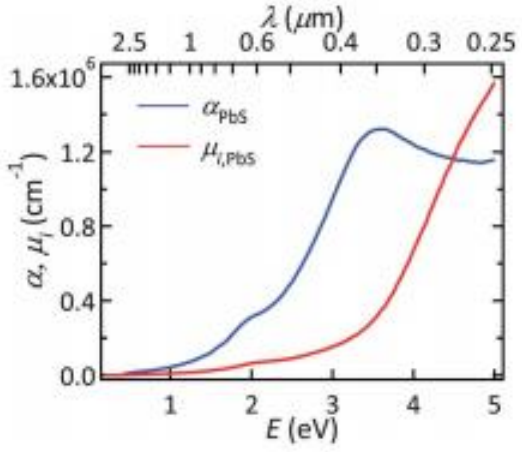

Figure 3: Absorption coefficient of bulk PbS (blue), and intrinsic absorption coefficient of PbS quantum dots (red) as functions of photon energy (bottom x axis) and wavelength (upper x axis) (17).

On the other hand, Fig. 4 (18) shows the absorption coefficient and absorption length of silicon as a function of photon energy and wavelength. As shown in the figure, absorption length of silicon in visible spectrum is on microns scale, which is much higher compared to quantum dots. Thus, devices based on quantum dots may be more feasible for solar cell and photodetection applications if quantum dot-based devices achieve comparable efficiencies with silicon devices.

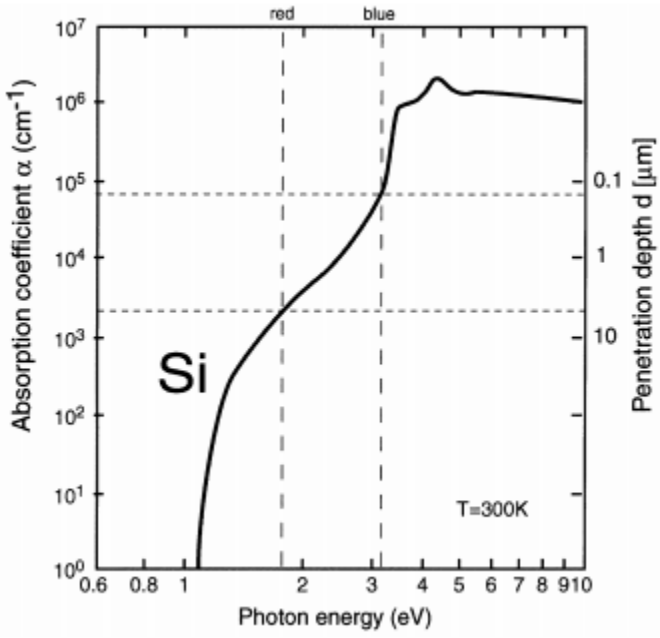

Figure 4: Absorption coefficient and penetration depth of silicon as functions of photon energy (bottom x axis) and wavelength (upper x axis) (18).

2.1.3 Structural Properties

The structure of quantum dots influences their optical properties, stability and their application area. Depending on the desired properties, core or core/shell quantum dots can be synthesized. One full coverage of core is called one monolayer shell. It is possible to cover core with multiple different shells as in the case of CdSe/CdS/ZnS, which means CdSe core is first covered with CdS shell, and then CdSe/CdS is covered with ZnS shell. Core can also be covered with same shell multiple times as in the case of InP/4ZnO, which means InP core is covered by 4 monolayers of ZnO shell. As mentioned in optical properties, shell coverage increases PL QY up to a certain coverage. After that point, further shell coverage increases the lattice strain so much that the strain

might start to cause dislocations in the crystal structure, which lead to more non-radiative recombinations, thus, decrease in PL QY (19-21).

It is commonly noted that QDs are more stable than organic semiconductors in terms of photobleaching and oxidation (22). Shells improve the stability of QDs considerably owing to passivation of surface defects and also prevention of oxygen diffusion into the core (23).

It is convenient to categorize QDs according to the energy band alignment of core and shell. In this regard, there are three types of core/shell energy alignment in QDs:

i) Type-I: In this type of QDs, core is covered with a larger band gap shell. Both electron and hole wavefunctions reside in the core as electron and hole energy is lower there. Type-I QDs are the most used QDs in LED applications mainly due to their high PL QY, strong confinement of electron and hole, and narrow emission spectra.

ii) Quasi-Type-II: Similar to type-I structure, both electron and hole are confined in the core because of larger band gap shell, however, one of the charge carriers tends to delocalize to the shells due to the similar energy levels between core and shell conduction band or valence band. In quasi-type-II structures, radiative lifetimes are longer compared to type-I structures as the electron-hole wavefunction overlap is lower, which means they can be separated more easily.

iii) Type-II: In this configuration, one charge carrier is confined in the core, while the other one is confined in the shell. Electron and hole wavefunctions barely overlap. As in Fig X, electrons have lower energy states in the conduction band of the shell, thus, the absorption occurs via core-shell transition of electrons. Similarly, since electrons reside in the shell, emission occurs via core-shell transition as well. That means absorption and emission energy get lower when core is covered with type-II aligned shell. Hence, type-II configuration causes a considerable red-shift in absorption and emission compared to core absorption/emission. As electron-hole wavefunction overlap is very low in type-II configuration, it is easier to separate electron and hole, which makes them convenient for solar cell and photodetector applications.

The energy alignment of core/shell structure for type-I, quasi type-II and type-II QDs together with the electron and hole wave functions are shown in Fig. 5 (24).

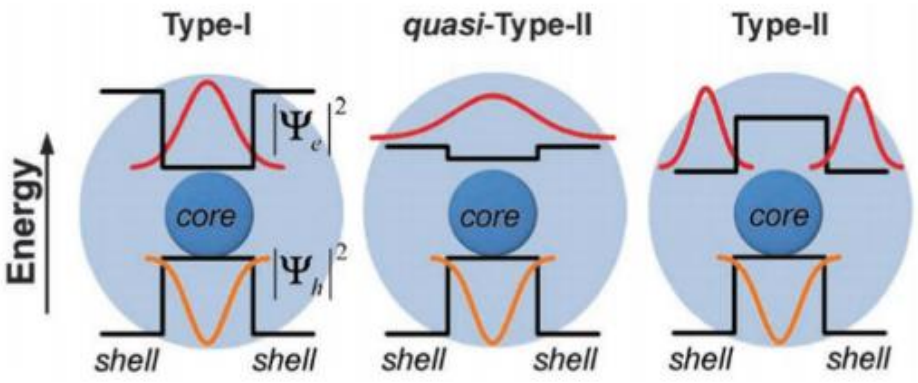

Figure 5: The energy alignments and electron-hole wavefunctions for type-I, quasi-type-II and type-II core/shell quantum dots (24).

2.2 QLEDs

Owing to the favorable electronic and optical properties of quantum dots, their application in light-emitting devices has attracted a lot of attention. Following the first demonstration of electroluminescent QLED in 1994 by Alivisatos et. al. (25), researchers have been conducting a lot of studies to increase the efficiencies of QLEDs by developing alternative QD synthesis methods, investigating different device architectures and discovering new materials.

2.2.1 Working mechanism of QLEDs

The motivation behind using quantum dots for LEDs originates from OLEDs. Operation, device structures, and the materials used in device structures of QLEDs are very similar to OLEDs. In QLEDs, a quantum dot layer is used as active layer compared to OLEDs which use an organic semiconductor layer as emissive layer. By electrically injecting charges into the device, electron-hole recombination in the quantum dot layer results in luminescence, or with a more common term electroluminescence. Thus, the aim is to collect as many of injected charges as possible in the quantum dot layer and make them stay in the active layer as long as possible. For this purpose, using charge transport/blocking layers is common in device architectures. Fig. 6a shows a typical device structure of a QLED. Electron transport layers with high electron mobility and hole transport layers with high mobility play crucial role in achieving high efficiency devices. Transport layers

facilitate higher charge injection, while also blocking the migration of opposite charge to the other layers. For example, hole transport layer allows hole transition to the active layer, while preventing electrons to leave active layer via its high conduction band energy level (Fig. 6b).

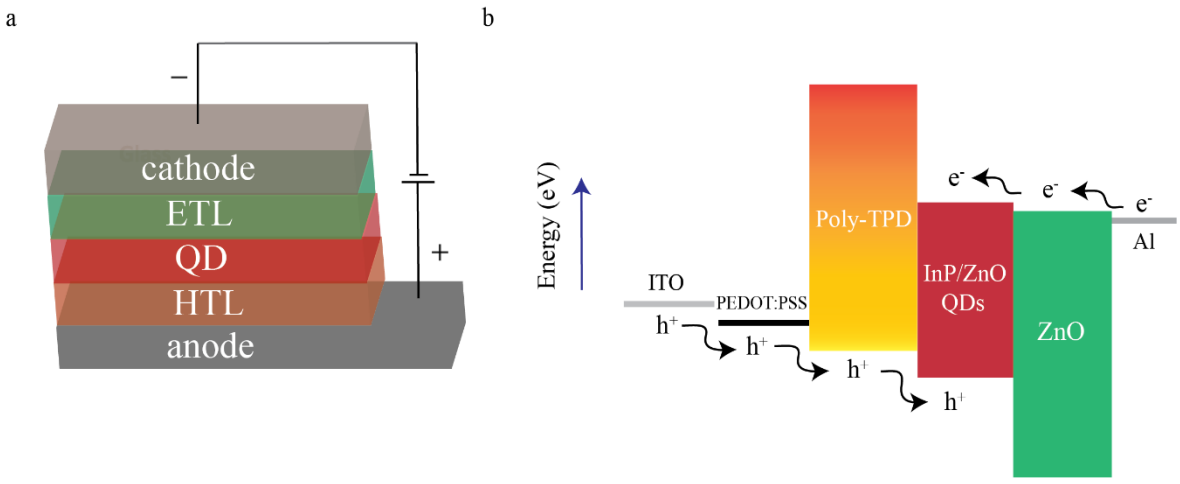

Figure 6: a) Typical device structure of multiple layered QLEDs. b) Energy band diagram of a typical QLED showing electron (filled circles) and hole (empty circles) movement in the device.

2.2.2 Fabrication of QLEDs

As QLEDs consist of multiple thin film layers coated on top of each other, the coating techniques used for the fabrication have great importance on the performance of LEDs. In the ideal case, the fabrication should be simple, cheap and high quality. However, typical fabrication methods used for QLEDs do not reflect the ideal case; they lack one or some of the advantageous properties. There are two main fabrication procedures, solution processing and physical vapor deposition (PVD), which were used in our studies and described here.

i) Solution Processing

Solution processing is the general name for several techniques (spin coating, dip coating, doctor blading, drop casting, etc.), in which a material is first dissolved in a solvent, and then coated to the substrate from its solution. Compared to PVD, solution processing is simple and cheap. On the other hand, the film uniformity and large-scale reproducibility may be problematic for these techniques in certain cases.

Spin Coating

Being the most common solution processing techniques and the one that was used extensively in our study, spin coating operates based on the centripetal force created due to a certain spinning speed. In this technique, an amount of solution is dispensed onto a substrate and the substrate is rotated with a certain spin speed. With the effect of spinning, the solution on the substrate is expelled from the substrate, and the layer gets thinner. After solution outflow stops due to spinning, the layer gets further thinner because of the evaporation of the solvent, and finally reaches to the desired thickness. The thickness of the layer depends on the spin speed, concentration of the solution, and the type of the solvent. As spin speed increases, the layer thickness decreases, and vice versa. Concentration of solution is a more effective parameter in the thickness of the film. The higher concentration yields a thicker film, and vice versa. Having different evaporation rates under same conditions, different types of solvents result in different thicknesses. For example, two common QD solvents, hexane and toluene, have different boiling points, 68°C and 110°C respectively. Thus, under same conditions, a solution with hexane results in different thickness and morphology of films compared to a solution with toluene.

ii) Physical Vapor Deposition (PVD)

In PVD methods, a material is first vaporized, and then the vaporized material is coated onto a substrate. PVD techniques generally provide more uniform coatings and higher level of control on the thickness of layers. However, they require more complex and expensive setup, and longer

coating durations compared to solution processing methods. We will briefly explain one of the PVD techniques, thermal evaporation, which we used to coat aluminum onto our substrates.

Thermal Evaporation

Thermal evaporation is a physical coating method used for many different materials. It is especially favorable for the coating of materials that have high boiling points such as metals in lower temperatures by decreasing the air pressure to 10^{-6}-10^{-7} Torr values. Thermal evaporation devices lower the pressure by vacuuming the air in their vacuum chamber, inside which the substrate and coating material are located. Coating material sits in a crucible, which is heated by applying AC current for the evaporation of the material. The evaporation rate can be controlled by changing the applied AC current to the crucible. It is possible to have coating rates even lower than angstroms. This enables a high-level control on film thicknesses.

2.2.3 Performance metrics of QLEDs

i) Current-Voltage Characteristics

After the fabrication of QLEDs, typically the first step of characterization is to take current-voltage (IV) or current density-voltage (JV) measurement. The observation of diode-like rectifying behavior in IV curve is the first verification of a working device. Besides, IV curve provides important information about turn-on voltage and charge carrier densities. In Fig. 7, a basic IV measurement setup is shown from our laboratory, which includes a Keithley instrument and a software.

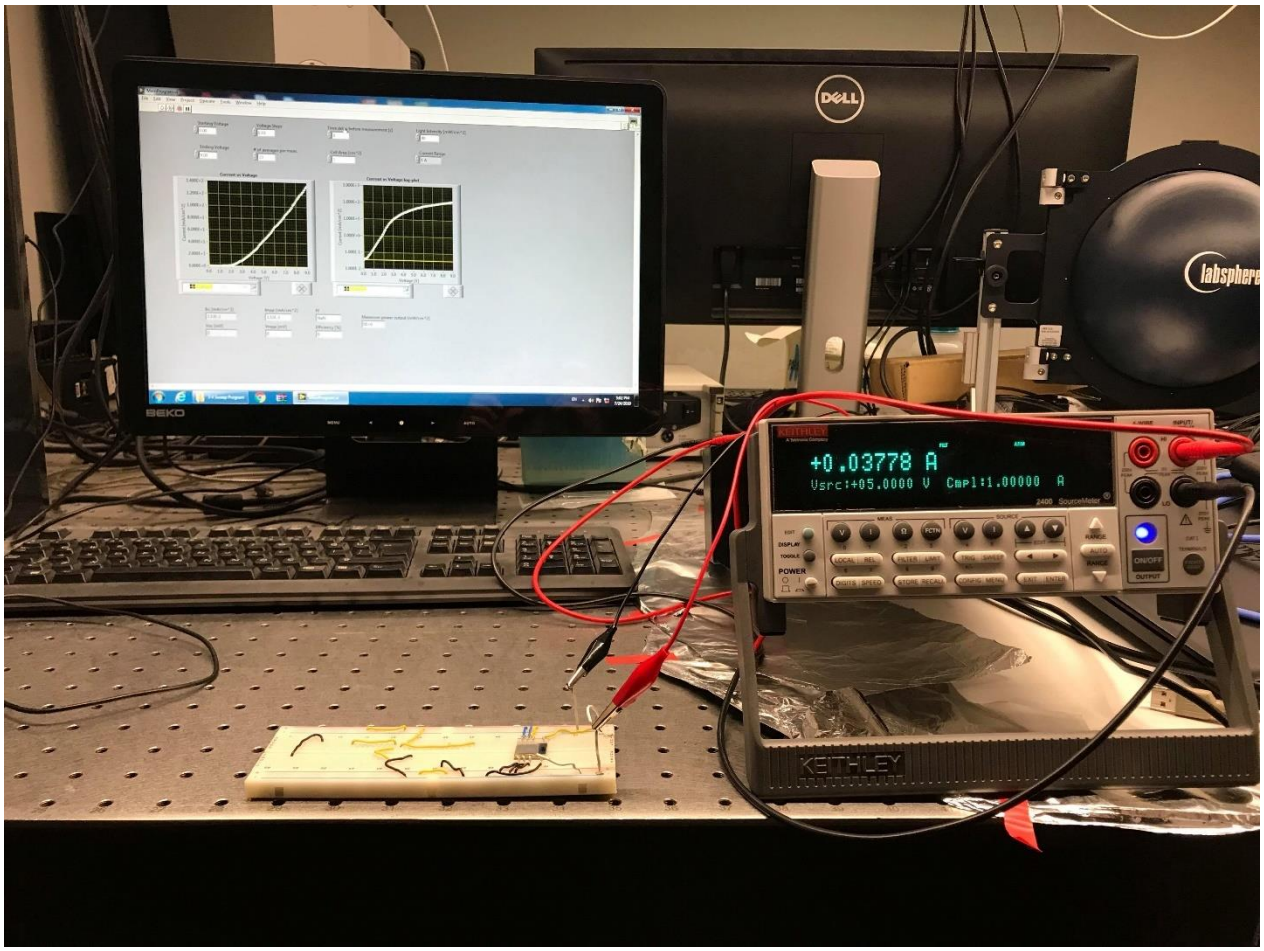

Figure 7: IV measurement setup with Keithley 2400 instrument.

ii) Luminous Efficiency & Luminance

Since the main application of QLEDs are in display technology and lighting, photometric quantities are used to characterize the light and color perception of the human eye. That is why photometric units depend on eye sensitivity function. Fig. 8 demonstrates the eye sensitivity function, V(λ) (26). According to V(λ), the human eye is most sensitive to 555 nm radiation. Electromagnetic radiations outside the 370 nm – 750 nm interval do not have photometric meaning as they are not perceived by the human eye.

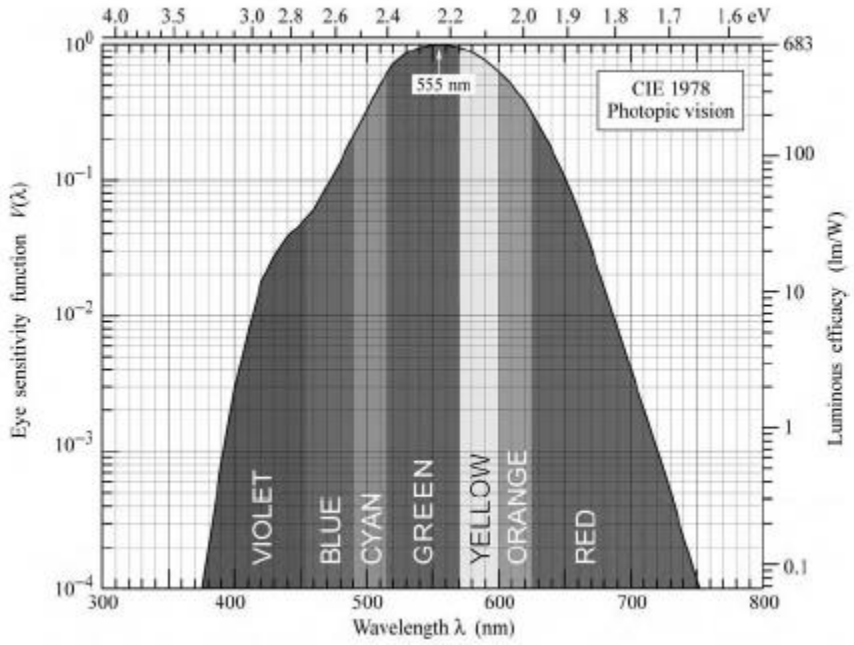

Figure 8: Eye sensitivity function, V(λ), defined according to Commission Internationale de l'Eclairage (CIE) 1978 standards (26).

Photometric quantities have great importance while evaluating the device performance. Luminous efficiency and luminance are the most reported photometric quantities in the literature. Luminous efficiency is the amount of luminous flux per electrical power used to drive the QLED. Its unit is lumens/watt (lm/W). Luminous flux is a measure of light power of a source perceived by the human eye and its unit is lumen (lm). The exact definition of lumen is the following: "a monochromatic light source emitting an optical power of (1/683) watt at 555 nm has a luminous flux of 1 lumen (lm)" (26). According to that definition, luminous flux can be written in the following form:

$$\Phi_{lum} = 683 \frac{lm}{W} \int_{\lambda} V(\lambda) P(\lambda) d\lambda \qquad (3)$$

where $P(\lambda)$ is the light power per unit wavelength, and $683\ lm/W$ is the normalization factor. Then, the luminous efficiency (LE) is written as following:

$$LE = \frac{\Phi_{lum}}{IV} \qquad (4)$$

where IV term represents the electrical power used to drive the device.

The luminance is the measure of luminous intensity per unit device area, and its unit is candela/m^2 (cd/m^2). The luminous intensity is the light intensity of an optical source perceived by the human eye. Its unit is candela (cd). Candela is defined as: "a monochromatic light source emitting an optical power of (1/683) watt at 555 nm into the solid angle of 1 steradian (sr) has a luminous intensity of 1 candela (cd)" (26). Based on that definition, 1 cd is equal to 1 lm/sr. The term "brightness" is also used as a synonym for luminance.

iii) External Quantum Efficiency

The ratio of the number of photons emitted out of the device per second to the number of electrons injected into the device per second is named as external quantum efficiency (EQE). It is one of the most crucial performance metrics for all types of LEDs. EQE depends on different efficiency parameters, and can be written as:

$$EQE = \eta_r \, \chi \, \eta_{PL} \, \eta_{OC} \qquad (5)$$

where η_r is the fraction of injected charges that form excitons in active layer (charge carrier balance factor), χ is the fraction of total excitons whose states have spin-allowed transitions, η_{PL} is the PL QY of the active layer material, and η_{OC} is the fraction of emitted photons that are coupled out of device (light out-coupling efficiency). Charge carrier balance factor η_r is related to the band alignment of the constituent materials and the balance of electron and hole injection into the QD layer. Hence, engineering the band alignment by proper material choices and careful investigation of energy levels and charge mobilities of charge transport layers are crucial to maximize η_r. χ is typically 1 for QDs, because transitions from spin-forbidden states to spin-allowed states occur frequently in room temperature for QDs. PL QY of the active layer material is typically taken as the QY of the solid film. When QDs in solution are condensed into a solid film, their QY drops. The amount of drop is considered around one order of magnitude for core-only QDs (27). To prevent the so called "self-quenching" of QDs when they are transferred into thin film, people synthesize QDs with thick shells (28). Thick shells decrease the separation between QD cores, which diminishes the energy transfer between them. Less energy transfer means less amount of QY drop for QD thin films (22). However, one needs to pay attention while synthesizing thick quantum dots, since the enhanced strain between core and shell can cause QY to diminish rapidly

after a certain shell thickness (29). Light out-coupling efficiency is the factor that limits the EQE of LEDs the most. Its value is around 20% for most LEDs (30). This is because nearly 80% of the light generated in the active layer cannot escape the device due to total internal reflection and waveguiding effects of other layers (31). Increasing the outcoupling efficiency is an important topic of study in LED research and many different strategies have been already proposed to enhance η_{OC}, some of which might be helpful for overcoming this problem (32-34).

CHAPTER 3 InP based QLED Fabrication & Results

3.1 Introduction

Consumer electronics industry is rapidly growing due to massive amount of demand. In parallel with this high demand, the electronic waste (e-waste) problem grows as well. The total e-waste generated worldwide was estimated to be around 41.8 million tones in 2014, and it is expected to reach 50 million tones in 2018.(2) Consumer electronic products are typically made of indecomposable, non-biocompatible and sometimes even toxic materials, which may pose serious threats to human health, variety of species and environment. The regulations regarding the use of such materials in consumer goods is getting stricter day by day. “Directive on the restriction of the use of certain hazardous substances in electrical and electronic equipment” (RoHS) and “Waste Electrical and Electronic Equipment Directive” (WEEE) by the European Union are examples of such regulations. Thus, the need for “green material” based devices that are environmentally friendly and biocompatible for electronics industry is rapidly increasing.

Lighting and display applications account for a considerable portion of electronics industry. For example, almost one-fifth of the electricity generated is being consumed by lighting applications.(35) Semiconductor based LEDs, organic LEDs, and more recently quantum dot light-emitting devices (QLEDs) have been increasingly used in such applications. Ever since the first demonstration of QLEDs (36), incorporating QDs as emissive layer in LED architectures has attracted significant attention.(37-40) This interest stems from the excellent optical and electrical properties of QDs such as high fluorescent efficiency, narrow emission spectra, low-cost solution processability and spectral tunability via quantum confinement effect.(41-45) QLEDs especially generated interest for lighting and display applications after reaching comparable performances with organic light-emitting diodes (OLED) and semiconductor based LEDs.(46-48) Up to now, the most well-understood and optimized QDs for LED applications are cadmium-based, because of their outstanding characteristics such as near unity photoluminescence quantum yield (PL QY), narrow full width at half maximum (FWHM) and well-developed size control that can cover full

visible spectrum. However, cadmium (Cd) is a highly toxic metal and Cd-containing systems can have significant negative effects on ecosystem.(9, 49) As a replacement of Cd-based compounds, many alternative QDs were proposed such as $CuInS_2$ (CIS), $AgInS_2$, ZnSe, and InP is one of the most suitable QDs for light-emitting applications owing to its high quantum yield and tunable band-gap. The previous studies on InP-based QLEDs were based on heterostructures with type-I core/shell QDs.(50-53) Application of type-II QDs to LEDs was demonstrated in very few reports, in which only toxic-heavy metal based QDs were used.(54, 55) Nontoxic InP-based type-II QDs have not been studied yet for QLEDs. This led us to use InP/ZnO QDs as active layer in QLED architecture. In the next sections, we will discuss the fabrication of InP/ZnO based QLEDs, characterization of QD nanostructure and device structure, and performance merits of optimized devices.

3.2 Device Fabrication

We fabricated the QLEDs by solution processing methods except the deposition of cathode material with thermal evaporation. The most part of the fabrication, including thermal evaporation takes place in the glove box, which has an inert atmosphere (Fig. 9).

Figure 9: Nitrogen glove box in our laboratory, where the most part of the QLED fabrication takes place.

Our typical fabrication procedure is as following:

The QLEDs were fabricated on glass substrates covered with patterned indium tin oxide (ITO). The substrates were first cleaned with detergent solution, acetone, DI water and iso-propanol, consecutively, for 15 min each, and then treated with UV generated ozone for 15 min to increase the work function of ITO and further eliminate the residues on the ITO surface. PEDOT:PSS (poly(3,4-ethylenedioxythiophene) polystyrene sulfonate) solution (filtered through a 0.45 um filter) was spin coated onto the ITO substrates at 4000 rpm for 45 s, and baked at 150°C for 15 min under ambient conditions. The PEDOT:PSS-coated substrates were transferred into a nitrogen-filled glove box for spin-coating of the poly(N,N9-bis-(4-butylphenyl)-N,N9-bis(phenyl)-benzidine) (poly-TPD) layer. Poly-TPD, used as hole transport layer (HTL) (8 mg/ml in chlorobenzene), was spin coated for 40 s and the spin speed was varied through 1000 rpm, 2000

rpm, 3000 rpm, 4000 rpm to obtain thicknesses of 60 nm, 50 nm, 40 nm and 30 nm respectively; followed by baking at 130°C for 30 min. After that InP/ZnO QD solution (10 mg/ml in toluene) was spin coated for 45 s and the spin speed was varied through 500 rpm, 1000 rpm, 2000 rpm and 4000 rpm to obtain thicknesses of 50 nm, 40 nm, 30 nm and 20 nm, respectively; and baked at 70°C for 20 min. For the deposition of electron transport layer (ETL), ZnO nanoparticles solution in ethanol with a concentration of 30 mg/ml was spin coated for 60 s, and the spin speed was varied through 1000 rpm, 2500 rpm, 4500 rpm and 6000 rpm to obtain thicknesses of 50 nm, 40 nm, 30 nm, and 20 nm, respectively; and baked at 90°C for 30 min. Finally, the top Al cathode layer (100 nm) was thermally deposited under a based pressure of 1 x 10^{-6} Pa. Devices were encapsulated before taking the measurements. Fig. 10 shows three sample QLEDs we fabricated in our lab, which are ready for test measurements.

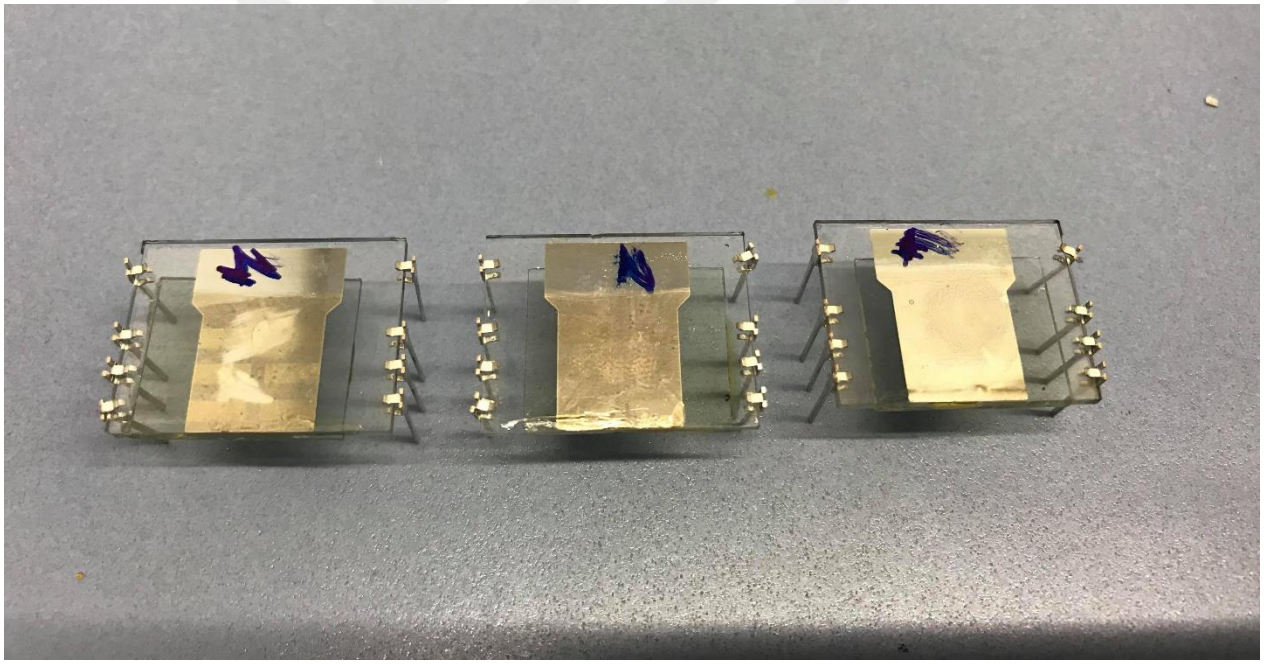

Figure 10: Sample encapsulated QLEDs fabricated in our lab. Connection legs were mounted for testing.

3.3 Optimization of QD nanostructure for QLEDs

Since the PL QY of the thin film is crucial for the EQE of QLEDs, we aimed to have low self-quenching by minimizing the reabsorption losses and energy transfer between QDs. Reabsorption occurs when an emitted photon by one QD is absorbed by another QD without leaving the device.

To decrease reabsorption, we need to have as low overlap as possible between absorption and emission spectra of QDs (56). Also, energy transfer can be decreased by increasing the distances between QD cores, which can be performed by having thicker shell.

As shown in the band alignment of InP/ZnO QDs in Fig. 12a, holes are confined in the core, while electrons tend to delocalize to the shell because of the similar electron affinities of the core and shell. Due to the quasi-type-II energy alignment of core-shell structure, the emission is dominated by recombination of core excitons, whereas the absorption is predominantly caused by the shell, which is especially the case for QDs with thick shell.(57, 58) This can be utilized to decrease the spectral absorption and emission overlap, which in turn reduces the reabsorption and also decreases PL efficiency drop of QDs in solid state. To this end, we synthesized InP core, InP/1ZnO and InP/2ZnO QDs for investigating the effect of shell thickness on the optical properties of QDs, whose synthesis details, core/shell formation procedure, structural details, and biocompatibility tests were provided in our previous studies (29, 59) (See also appendix section for synthesis description). Fig. 12b provides the absorption and emission spectra of synthesized QDs. With increasing shell thickness, we observe a red shift in the emission peak wavelength expectedly due to the progressive delocalization of electron wavefunction to the shell, which induces a decrease in the degree of spatial confinement for electron.(60, 61) As a result, having a higher Stokes shift between PL and absorption, the minimum reabsorption is achieved for InP/2ZnO QDs. Since a thicker shell also increases the central distances between individual QDs, it reduces the energy transfer among QDs, which is strongly dependent on inter-dot spacing.

To experimentally show that the energy transfer decreases as the shell gets thicker, we performed time-resolved PL measurements of InP core, InP/1ZnO and InP/2ZnO QDs to investigate the PL decay dynamics in film (Fig. 11). We observed that the lifetime is considerably higher for InP/1ZnO (3.8 ± 0.2 ns) compared to InP core (2.46 ± 0.09 ns). Similarly, lifetime for InP/2ZnO (4.52 ± 0.34 ns) is higher than InP/1ZnO (3.8 ± 0.2 ns). This result implies that thicker shell plays a role as an extra spacer that increases the distance between cores and suppresses energy transfer among them. Similar behavior can be observed in Cd-based counterparts as well. (62-64)

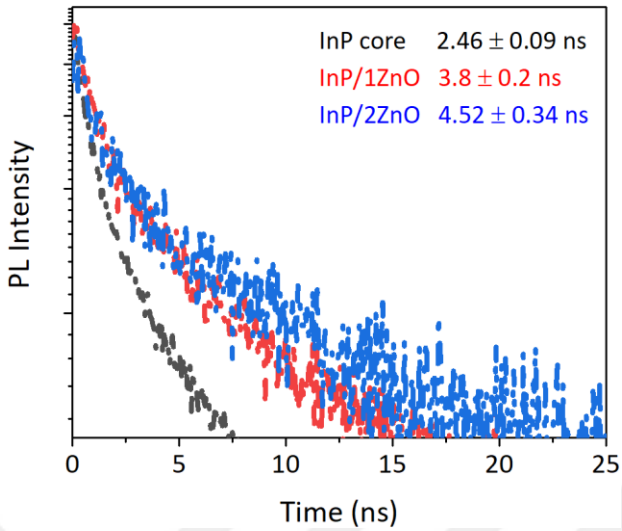

Figure 11: PL decay dynamics of solid films of InP core, InP/1ZnO, and InP/2ZnO QDs.

Sample	**A_1 (kCnts)**	**A_2 (kCnts)**	**A_{SUM} (kCnts)**	**τ_1 (ns)**	**τ_2 (ns)**	**τ_{avg} (ns)**
InP Core	3.18±0.21	9±1	12.5±1.1	6.39±0.23	1.121±0.043	2.46±0.092
InP/1ZnO	0.475±0.056	0.79±0.13	1.26±0.18	7.95±0.57	1.27±0.11	3.8±0.2
InP/2ZnO	0.92±0.04	1.24±0.18	2.17±0.16	8.9±0.79	1.31±0.26	4.52±0.34

Table 1: PL decay analysis of InP core, InP/1ZnO and InP/2ZnO.

Average lifetimes was calculated from amplitude average mean (65):

$$\tau_{avg} = \frac{A_1\tau_1^2 + A_2\tau_2^2}{A_1\tau_1 + A_2\tau_2} \qquad (6)$$

Quantum yields of the QDs must be particularly considered for LED applications. It is noted that the QY can be significantly enhanced by growing multiple shells around the QD core, owing to better passivation of surface trap states.(66) However, in case of further increasing the shell thickness after certain coverage, the QY starts to decrease like in CdSe/CdS core/shell nanostructures (67), possibly due to the strain caused by lattice mismatch (of %11 in this study (59)) between core and shell. This is what we observe in Fig. 1c, which presents the absolute quantum yields of InP core, InP/1ZnO and InP/2ZnO QDs in solution and after spin-coating them onto the glass substrate. The QY (in solution) improves from 8% to 30% after 1 ML coverage, but

then it diminishes dramatically to 12% after further 2 MLs coverage. Similar behavior can also be observed in both cadmium-based and indium-based counterparts.(21, 67) Consequently, even though InP/2ZnO has lower percentage of efficiency loss (20%) in comparison with InP/1ZnO QDs (30%) when transferred into thin film, this drop is acceptable considering one order of magnitude loss reported in the literature, and still InP/1ZnO QDs show higher in-film efficiency of 21%.(68) Hence, InP/1ZnO appeals as an appropriate emissive layer for LED application considering its higher QY and also its rather low efficiency loss in solid state.

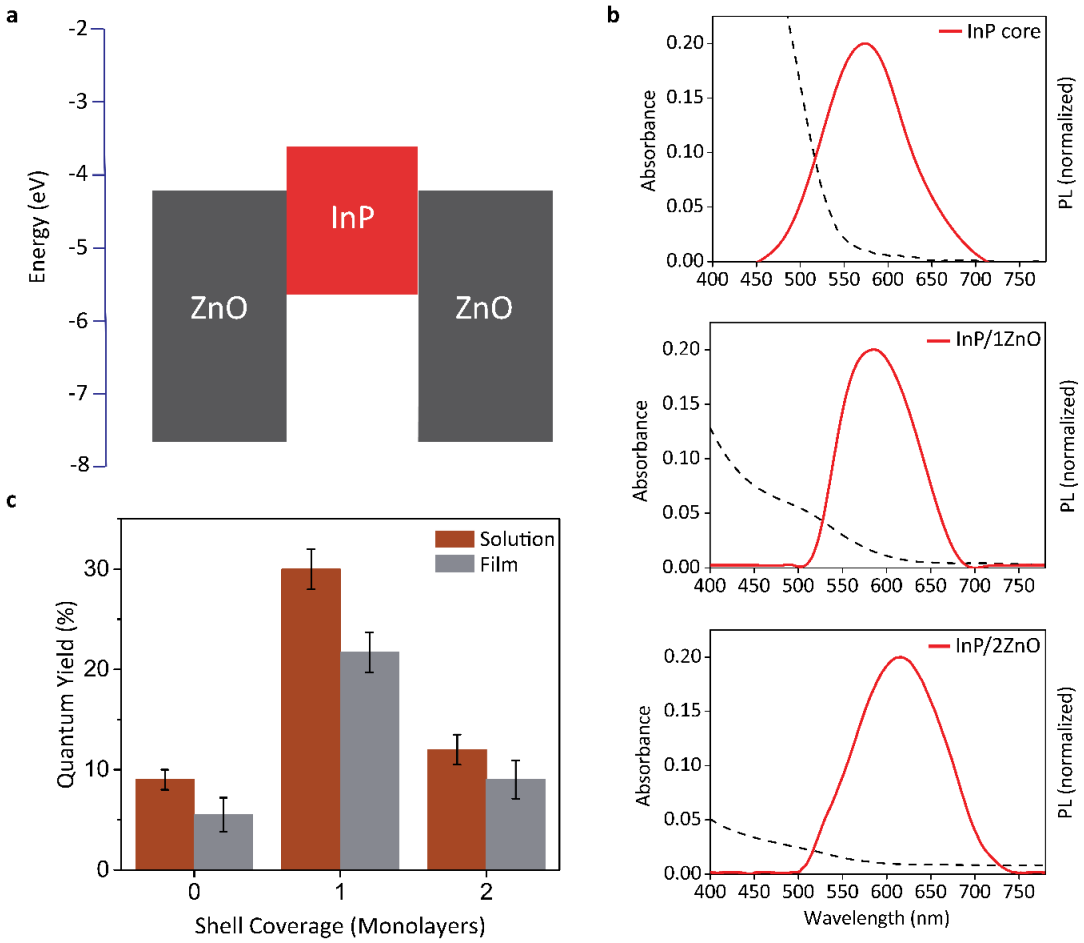

Figure 12: a) InP/ZnO core-shell QD having type-II energy band alignment.(60) b) Absorption (dashed line) and emission (solid line) spectra of InP core, InP/1ZnO and InP/2ZnO QDs (Tauc plots for each QD can be seen in appendix). c) Absolute quantum yield measurements of InP core, InP/1ZnO and InP/2ZnO QDs in solution and in film (N=3).

3.4 Device Structure and Band Alignment

The device structure of fully solution processed and bottom-emitting QLEDs consists of the following layers on a glass substrate: a transparent indium tin oxide (ITO) electrode, poly(ethylenedioxythiophene)-polystyrene sulfonate (PEDOT-PSS), poly(N,N9-bis-(4-butylphenyl)-N,N9-bis(phenyl)-benzidine) (Poly-TPD), InP/1ZnO core/shell QDs, ZnO nanoparticles, and the top Al electrode, which is shown in Fig. 13a (The details of synthesis of QDs, and synthesis of ZnO nanoparticles are provided in appendix section). As expected from the energy band diagram of Fig. 13b, Poly-TPD is chosen as HTL due to the lower highest occupied molecular orbital (HOMO) energy level of -5.4 eV (69, 70) and a high hole mobility, which are in favor of the hole injection and transport, and also higher lowest unoccupied molecular orbital (LUMO) energy level of -2.2 eV (69, 70), which helps to increase the recombination rate by confining electrons within the QD layer due to the rather large energy offset (~1.5 eV) at Poly-TPD/QD interface. ZnO is chosen as ETL due to high electron mobility, large valence band offset at the QD/ZnO interface (~1.5 eV), and efficient electron injection ability with electron affinity of ~4.11 eV and ionization potential of ~7.22 eV (Ultraviolet Photoelectron Spectroscopy measurements of InP/ZnO QDs and ZnO nanoparticles can be seen in Fig. 14 and Fig. 15).

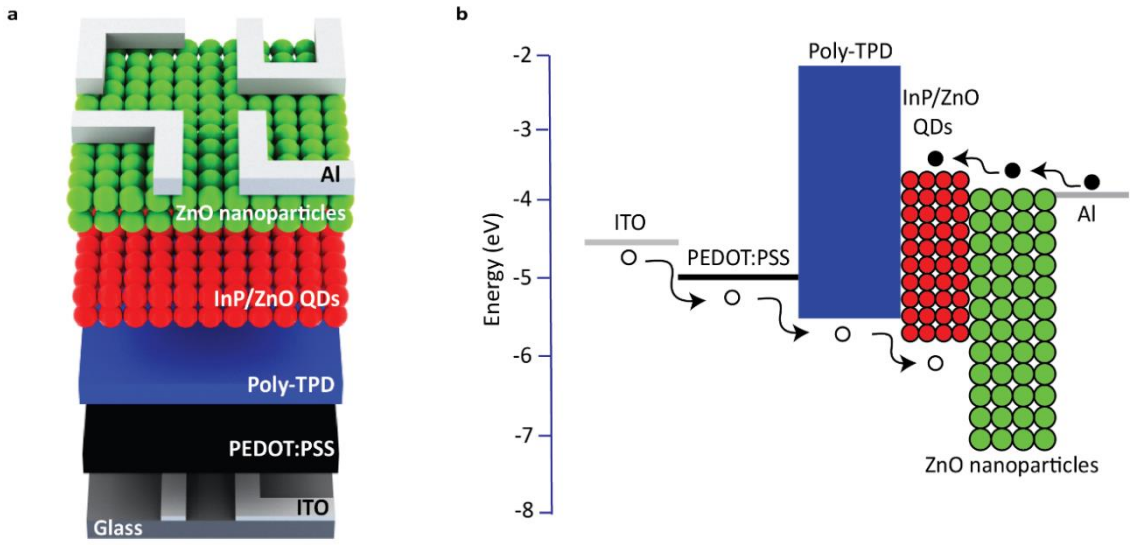

Figure 13: a) Schematic of multilayered device structure. b) Energy band diagram for constituent layers. The displacement of electrons (filled circles) and holes (empty circles) is shown.

UPS measurements of InP/ZnO QDs and ZnO nanoparticles

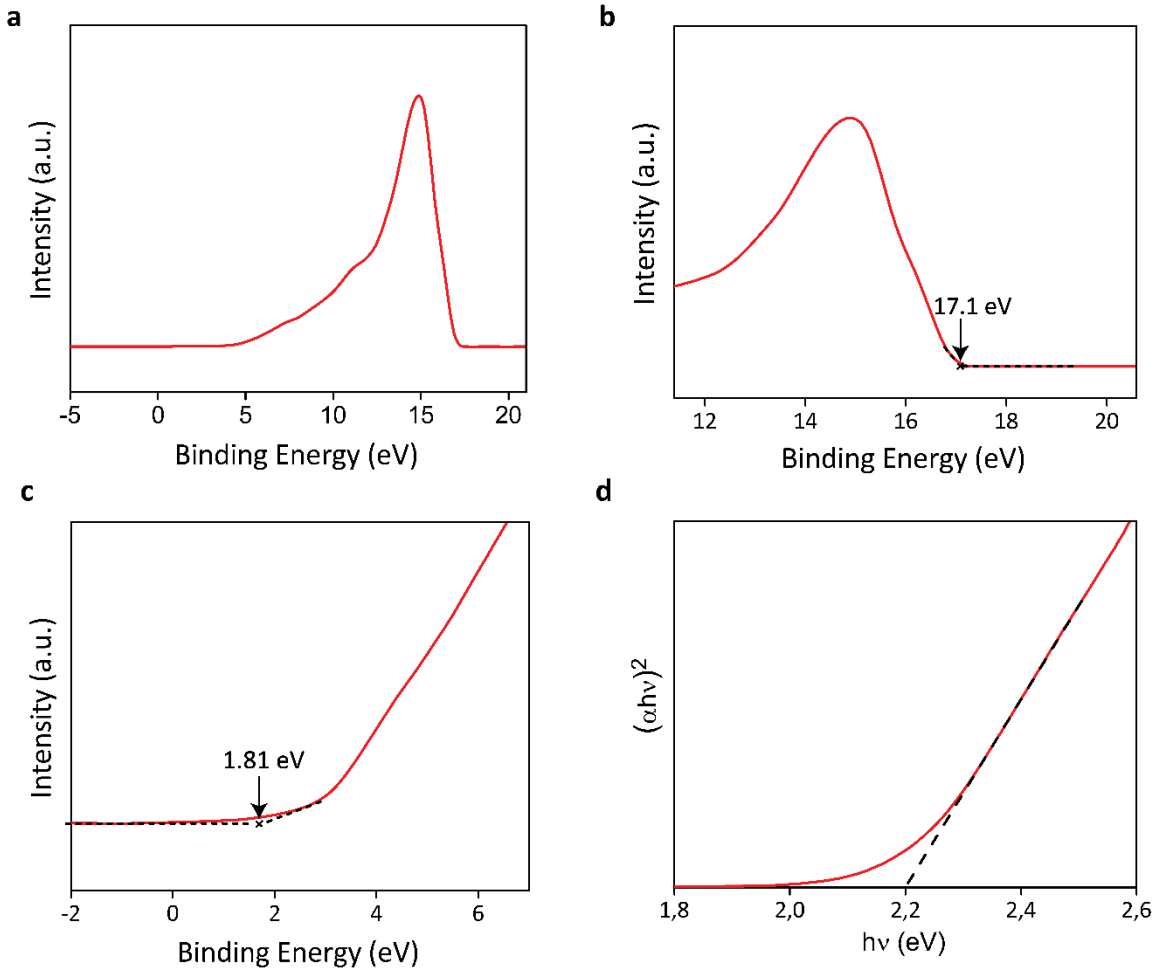

Figure 14: a) UPS spectra of InP/ZnO QDs. b) Zoomed-in secondary electron cutoff region. c) Zoomed-in valence band region. d) Tauc plot of InP/ZnO QDs showing optical band gap of 2.2 eV.

Figure 14a shows the whole UPS spectrum of InP/ZnO QDs. We obtain the work function(ϕ) using

$$\phi = hv - E_{cutoff} \qquad (7)$$

$hv = 21.22\ eV$ as HeI source is used, and $E_{cutoff} = 17.10\ eV$ from Fig. 14b, which gives us $\phi = 4.12\ eV$. Fig. 14c shows the valence band region, from which we obtain valence band energy level, $E_{vb} = 4.12\ eV + 1.81\ eV = 5.93\ eV$. We also calculated optical bandgap from tauc plot (Fig. 14d), which is 2.2 eV. This gives conduction band level as $E_{cb} = -5.93\ eV + 2.2\ eV = -3.73\ eV$.

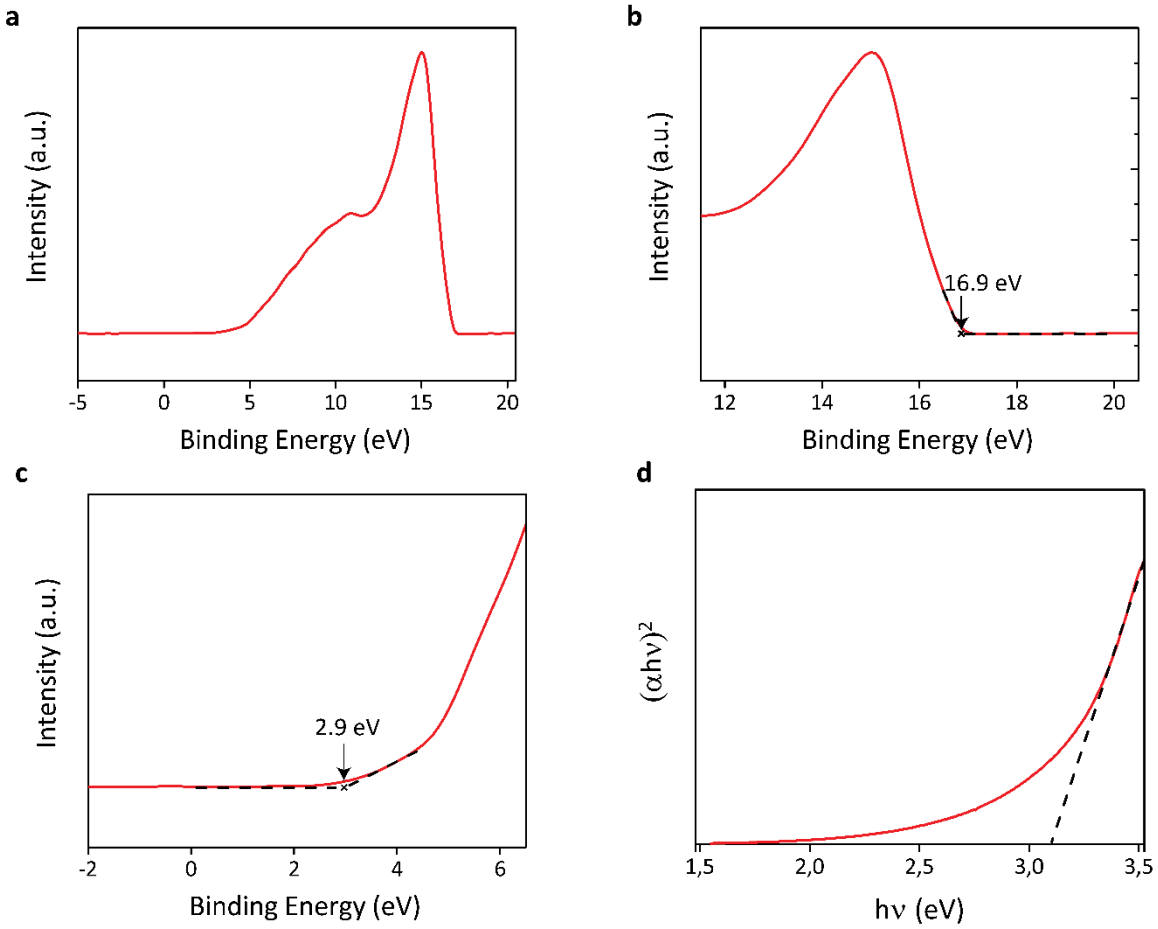

Figure 15: a) UPS spectra of ZnO naonparticles. b) Zoomed-in secondary electron cutoff region. c) Zoomed-in valence band region. d) Tauc plot of ZnO nanoparticles showing optical band gap of 3.1 eV.

Fig. 15a shows the whole UPS spectrum of ZnO nanoparticles. From the secondary cutoff region in Fig. 15b, we obtain the work function as $\phi = 21.22\ eV - 16.90\ eV = 4.32\ eV$. Then, we calculate valence band level from Fig. 15c as $E_{vb} = 4.32\ eV + 2.90\ eV = 7.22\ eV$. Finally, we obtain conduction band energy by adding optical band gap using tauc plot in Fig. 15d. $E_{cb} = -7.22\ eV + 3.11\ eV = -4.11\ eV$.

Energy diagram of hole transport layer, emissive layer and electron transport layer as a result of UPS measurements:

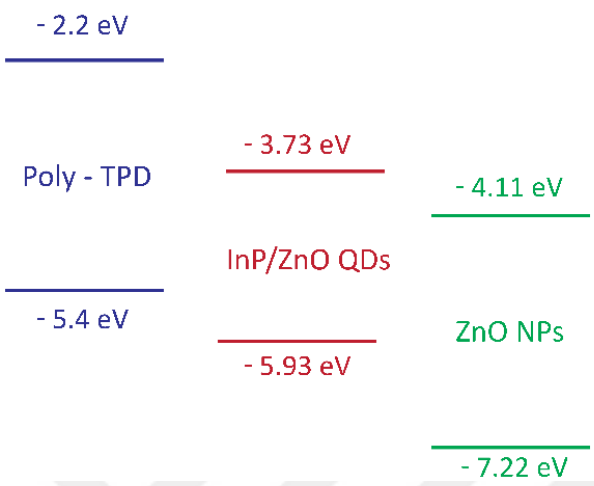

Figure 16: Energy diagram drawn as a result of UPS measurements of InP/ZnO QDs and ZnO nanoparticles, showing the energy barrier for electrons and holes as 0.38 eV and 0.53 eV, respectively.

3.5 Layer Optimizations

The device performance is highly dependent on the thicknesses of charge transport layers (CTL) and QD layer.(71) Thicknesses of charge transport layers have an impact on the efficient charge injection into the emissive layer, thus, optimization of HTL and ETL thicknesses enhances device efficiency by enabling recombination to take place predominantly within the QD layer. Fig. 17a demonstrates the current efficiency and external quantum efficiency (EQE) of the devices as a function of Poly-TPD layer thickness. The maximum efficiencies are achieved at 40 nm thickness with current efficiency of 1 cd/A and EQE of 0.53%. Further increase in the HTL thickness causes device efficiency to decrease due to more parasitic emission from Poly-TPD. As expected, the efficiencies are more sensitive to ETL thickness than HTL thickness due to the interference effect of the reflected light from the cathode.(72) As seen in Fig. 17b, increasing the ZnO layer thickness from 20 nm to 40 nm leads to nearly two-fold improvement in EQE. The current efficiency is less affected by ETL thickness, since luminance and current density vary proportionally to each other. After 40 nm, the device efficiency starts to drop upon further increasing the ETL thickness. Optimization of QD layer thickness is also required; and we measured the current efficiency and EQE for 20 nm, 30 nm, 40 nm and 50 nm QD layer thickness. On the one hand, while QD layer

gets thinner, it decreases the device efficiency by inducing higher leakage currents through voids and spaces between QD monolayers; on the other hand, while QD layer gets thicker, it makes charge transportation to QDs more difficult. (73) Based on the results in Fig. 17c, the optimal thickness for QD layer is determined to be 30 nm.

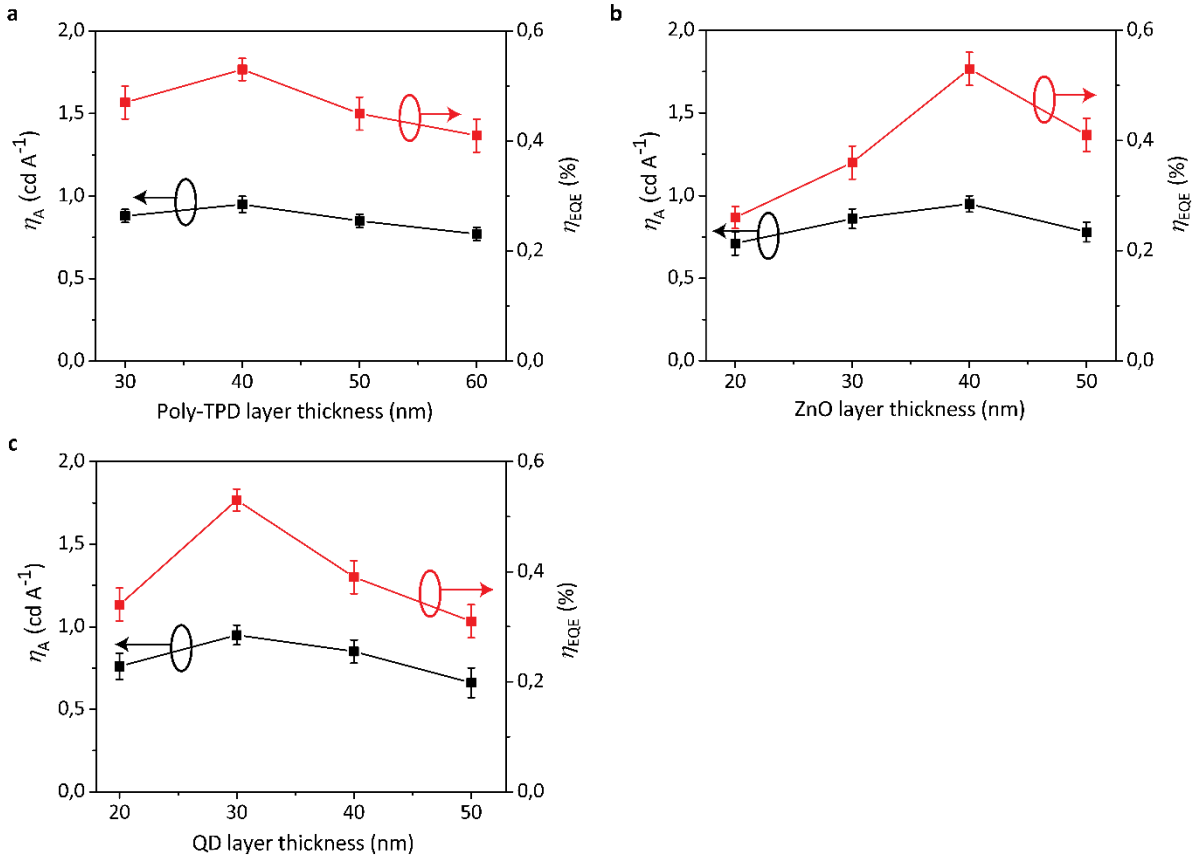

Figure 17: Current efficiency and EQE of the QLEDs as a function of a) Poly-TPD layer thickness (ZnO and QD layer thicknesses were kept constant at 40 nm and 30 nm, respectively), b) ZnO layer thickness (Poly-TPD and QD layer thicknesses were kept constant at 30 nm and 40 nm, respectively). Error bars represent the measurement variations for the average of 3 different devices. Different thicknesses were achieved by changing the spin speed.

3.6 Device Performance

Fig. 18a presents current density-luminance-voltage characteristics of the optimized QLED devices. We observe a low 2.8 V turn-on voltage, which is defined as the voltage at which luminance reaches 1 cd/m^2, due to efficient band alignment with 0.53 eV offset at HTL-QD interface and 0.38 eV offset at QD-ETL interface (Figure S3), which can be easily overcome by

electrons and holes under forward bias. Also, unlike type-I core/shell QDs for which electrons and holes need to overcome the energy barrier of the shell to reach the core, type-II QDs do not constitute an energy barrier for one type of charge (electrons in our case), which is another reason for achieving low turn-on voltage in our QLEDs. In Fig. 18a, maximum luminance reaches up to 600 cd/m^2 which, to the best of our knowledge, is the second highest luminance up to date among red InP based QLEDs.(52, 53) This is mainly due to efficient charge injection and recombination with optimized layer thicknesses and low PL quenching of type-II QDs when they are condensed into solid film state. The maximum luminance can further be improved by increasing the in-solution PL QY of InP/ZnO QD structures.

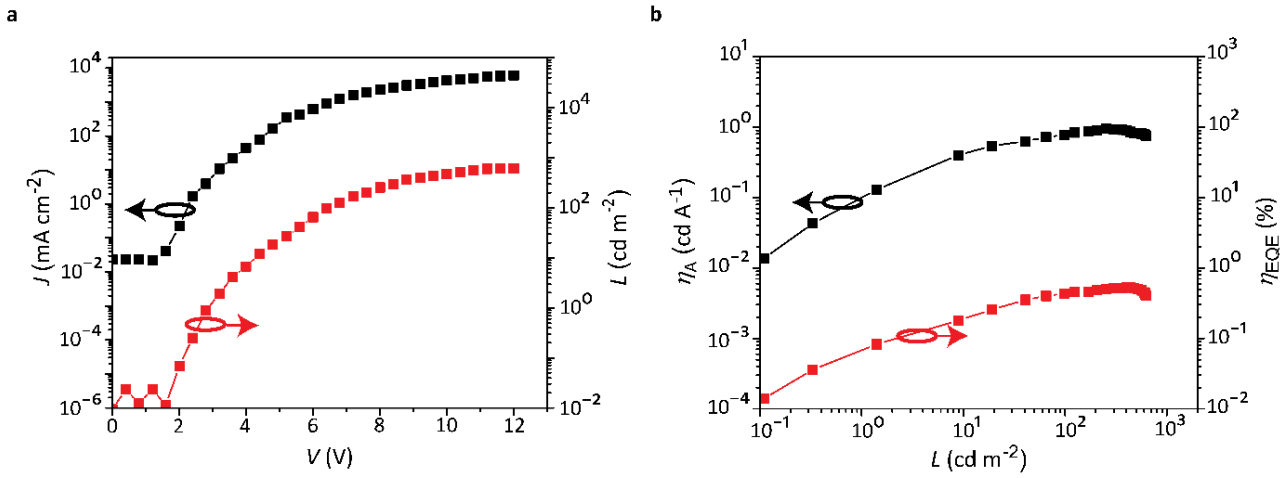

Figure 18: a) Current density-voltage-luminance (JVL) characteristics of the QLEDs (JVL characteristics of QLEDs with InP core, InP/1ZnO and InP/2ZnO can be seen in Fig. S6). b) Current efficiency and EQE of the QLEDs as a function luminance.

Current efficiency and EQE of the QLEDs as a function of luminance are seen in Fig. 18b. Highest current efficiency is achieved with 1 cd/A at a luminance of 300 cd/m^2. This luminance value is at convenient levels for display applications, which typically require 10^2-10^3 cd/m^2 luminance, but it needs to be increased for lighting applications, which require 10^3-10^4 cd/m^2 luminance.(49) After that point, although luminance keeps increasing up to 600 cd/m^2, current efficiency decreases due to parasitic emission from Poly-TPD. EQE is one of the most crucial EL characteristics for QLEDs. It is defined as the ratio of the number of the photons emitted by the device per unit time to the number of electrons that are injected per unit time, and formulized as: (49)

$$EQE = \eta_r \, \chi \, \eta_{PL} \, \eta_{OC} \qquad (8)$$

where η_r is the fraction of injected charges that form excitons in active layer (charge carrier balance factor), χ is the fraction of total excitons whose states have spin-allowed transitions, η_{PL} is the PL QY of the active layer material and η_{OC} is the fraction of emitted photons that are coupled out of device (light out-coupling efficiency). Due to the structural similarity between QLEDs and OLEDs, we expect our devices to result in a similar out-coupling efficiency value. It is known that in planar devices approximately 50% of the emitted light is generally lost in waveguided and plasmon modes. Other 25% is trapped in the substrate due to total internal reflection and around 5% is absorbed. The remaining 20% of the emitted light is the out-coupling fraction, η_{OC}.(33, 74, 75) PL QY of the active layer is 20% in our QLEDs. The value of χ is 25% and 75% for fluorescent and phosphorescent materials, respectively, and it can essentially be increased for fluorescent materials by certain mechanisms such as thermally activated delayed fluorescence. For QDs, transitions from dark to bright band-edge excitonic state frequently take place even at room temperature due to the small energetic barrier between dark and bright excitonic states, which is on the order of 8-10 meV for InP.(76, 77) Thus, the value of χ for QDs approaches 1 owing to the efficient crossings of excitons from dark states, in which spin-forbidden transitions to ground state occur, to bright states, where spin-allowed transitions to ground state take place. Based on these rational assumptions (i.e., χ is nearly 1 and η_{OC} is nearly 20%), and considering the maximum 0.53% EQE of our QLEDs, we obtain the value of η_r around 20%. In principle, it is possible to achieve values close to 1 for charge carrier balance factor, and in fact, there are some studies that get very close to that.(78, 79) However, for our devices, even though the layer thicknesses are optimized, we think there are two main factors that prevent the achievement of such high charge carrier balance factor: i) electron delocalization to shells decreases the probability of electron and hole wavefunction overlap, ii) high dielectric constant of InP reduces the strength of attractions between opposite charges.

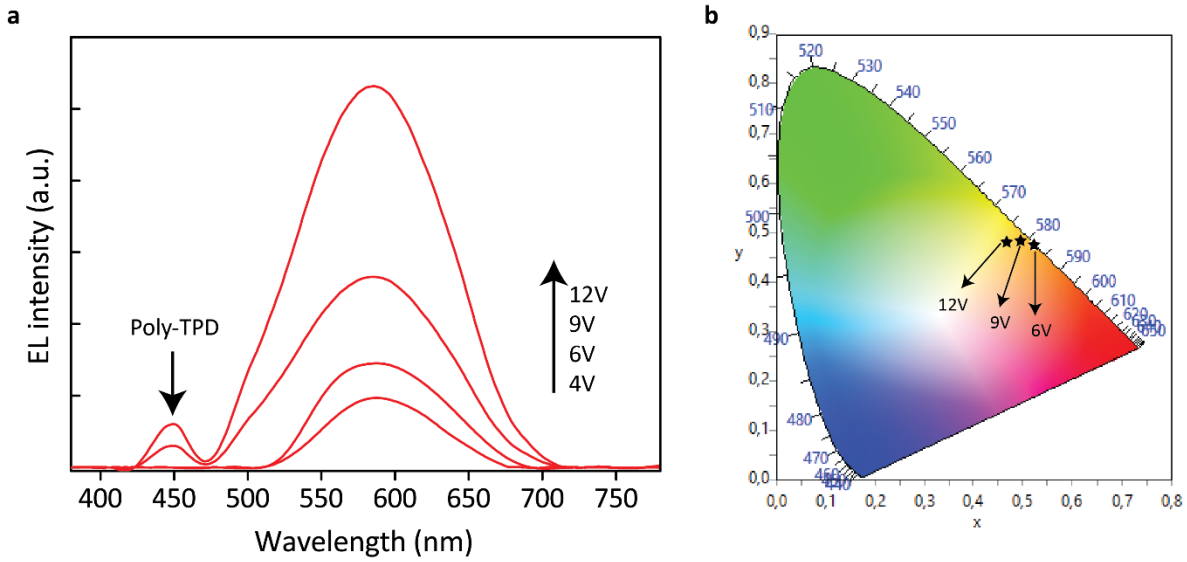

Figure 19: a) Electroluminescence spectra of the QLEDs at different biases. b) CIE coordinates of the emission at 6V, 9V and 12V.

The electroluminescence spectra of the QLEDs at operation voltages of 4V, 6V, 9V and 12V are shown in Fig. 19a. The emission peak wavelength is 585 nm and full width at half maximum (FWHM) is around 90 nm. We observe a weak emission in blue-wavelength region starting from 9V forward bias, which is originating from Poly-TPD layer. This blue emission can be ascribed to the small number of electrons attaining sufficient energy to overcome the energetic barrier at Poly-TPD-QD interface. As a result, this leaky emission leads to a widening in the lower wavelength region of the EL spectrum. At low voltages up to 8V, our devices exhibit saturated and pure colors with (x, y) tristimulus coordinates of (0.52, 0.47) as demonstrated by the Commission Internationale de l'Eclairage (CIE) chromaticity diagram shown in Fig. 19b. In the same figure, we also observe that with increasing voltage, appearance of leaky blue emission causes a shift in the color coordinates and affects color saturation adversely.

3.7 Conclusion

In summary, we presented the application of environmentally benign, biocompatible, type-II core/shell InP/ZnO QDs to LEDs for the first time. Investigation of PL QY in solution and in film showed that the efficiency loss of QDs when they are transferred into film is exceptionally low

owing to the ability of low reabsorption and energy transfer losses because of multiple shells on the core. We determined that the optimum choice for LED application is InP/1ZnO, which is InP core with 1 ML ZnO coverage, due to its high efficiency in solid state. Integrating InP/1ZnO as emissive layer into the fully solution processed LED architecture, our devices displayed low turn-on voltage of 2.8 V and saturated emission color with promising performance levels up to current efficiency of 1 cd/A and EQE of 0.53%. This study presents a new opportunity for the ability of engineering non-toxic QDs for minimizing solid-state efficiency loss by forming shells owing to type-II band alignment, and demonstrates luminance levels, which is suitable for display applications. Moreover, engineering toxic-content-free QDs at nanoscale in new architectures offers a significant room for further progress. Therefore, the results point to a novel direction in using eco-friendly quantum dots for light-emitting devices.

CHAPTER 4 QD based Biointerfaces for Neural Stimulation

4.1 Introduction & Background

Activation of neurons for treatment purposes commonly employs electrical stimulation using extracellular electrodes. Over the years, intensive studies have been undertaken in order to improve the electrical and mechanical interfacing between electrodes and neuronal tissues. However, extracellular electrodes are still lacking high spatial resolution, biocompatibility, flexibility and surgical difficulties due to the wirings and mechanical limitations.

An alternative approach to achieve neuronal activation is through light directed stimulation. Compared with the electrical stimulation techniques, optical methods for manipulating neuronal activity offer many advantages. Light can be easily focused to a fine spatial resolution, which enables flexibility in targeting single neurons and even discrete regions of a single neuron. When used within safe limits, light as a stimulation tool allows temporally and spatially precise activation of neurons, both in vitro and in vivo application, and can be used in biomedical applications such as drug screening, basic neuroscience investigations and neural implants, in particular for retinal implant applications.

Two main routes are most commonly used to optically activate neurons. The first is optogenetics, which is conducted through genetic manipulation of neurons, making them photosensitive by introducing light sensitive membrane proteins to neuronal cells. The second approach is controlling neuronal activity through photoactive interfaces. Photoactive interfaces create electrical signals in response to light. This way, it is possible to manipulate neuronal activity, which can be monitored by different methods such as calcium imaging and electrophysiology. Since optogenetics requires genetic modification, its use in human biology raises concerns. In this work, we focused on designing effective photoelectrodes that contain QDs as photoactive layer to stimulate neurons via light. We will discuss photoactive surfaces briefly before presenting our results.

4.1.1 Photoactive Surfaces

Photoactive interfaces make use of a photoactive material to convert incoming light into electrical current. This phenomenon, also called photoelectric effect, occurs via creation of electrons and holes in the photoactive material as a result of absorbed photons. Photons have a certain energy which is proportional to their frequency and can be written as following:

$$E = h\nu \qquad (9)$$

where h is the Planck's constant and ν is the frequency of the light. When a photon with a certain energy hits on a material which has a bandgap energy of equal or less than the photon's energy, that photon would be absorbed by transferring its energy to an electron, which goes to the excited state leaving a hole in its place. Electrons and holes prefer to stay in a lower energy state, thus, if there is an available state with a lower energy nearby, they would move to that energy state. Therefore, if one can create a system that would cause electrons and holes to move in opposite directions due to the alignment of energy states, electrical current can be created. Then, that current can be used to stimulate neurons, which are grown on top of the photoactive surface.

Since in this case neurons are not connected to the surface with a wire, this kind of stimulation is called wire-free photostimulation. The neurons on the surface of a photoactive material get stimulated due to the electric field created by the rapid movement of charges in the photoactive material or due to the faradaic reactions occurring in the extracellular medium due to the accumulated charges on the photoactive surface. The former type of stimulation is called capacitive stimulation, while the latter one is called faradaic stimulation. Capacitive stimulation is considered a safer method for the activation of neurons, because it does not change the concentration of ions in the extracellular medium (80). On the other hand, faradaic reactions change the ionic concentrations in the medium, which in turn may change the pH or temperature of the medium, consequently damaging the neurons.

Different types of materials can be used for photostimulation of neurons. Silicon, semiconducting polymers and quantum dots are some examples of the materials that have been studied for optical stimulation of neurons (81, 82). Also, there are plenty of different methods for the fabrication of optoelectronic neural interfaces, and all have their own advantages/disadvantages. Both physical deposition and solution processed fabrications can be encountered in the literature. Thermal

evaporation, chemical vapor deposition, spin coating and dip coating are some of the fabrication methods that have been used in different studies. While physical deposition methods enable more controlled, stable and uniform fabrication process, solution processed methods are easier, cheaper and faster. Fig. 20 (83) shows a photoactive biointerface which uses P3HT:PCBM as photoactive material. Neuronal cells are cultured on top of the devices. As a result of illumination, charge separation occurs in P3HT:PCBM layer. This triggers the change of electron concentration on the surface and in the medium, which affects the cell membrane potential.

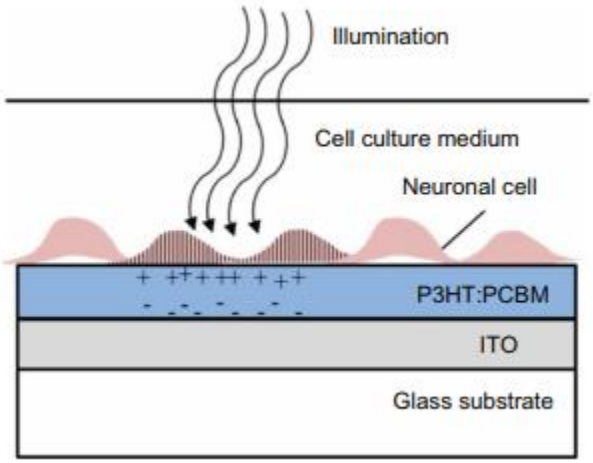

Figure 20: Typical neural photostimulation setup with a photoactive surface (P3HT:PCBM in this case) (81).

4.1.2 QD based photoactive surfaces

QDs have outstanding properties that make them suitable for photoactive interfaces. Tunable band gap provides flexibility for using QDs in different structures depending on the device energy band alignment. Solution processability of QDs enables simple and cheap fabrication procedures. Owing to their nanoscale size, QDs can be used for localized stimulation of small areas. Moreover, high absorption coefficient of QDs allows the fabrication of thinner devices, on the order of hundreds of nanometer thickness, that simplifies the surgical procedure of implants and provides accessibility to certain regions in the body, which would not be possible with larger-sized implants. Despite these advantages, there are only a few reports in the literature that use QDs for the stimulation of neurons.

In his pioneering work, Kotov et. al. showed photostimulation of NG108 neurons which are grown on a layer-by-layer structure of PDDA-HgTe QDs on ITO substrate (84). The thin films of HgTe QDs successfully depolarized the neurons with illumination, which then triggered action potentials. Afterwards, Lin et. al. fabricated CdSe QD films on ITO substrate, and grew mice cortical neurons on CdSe thin films (85). By illuminating the devices with blue light, they stimulated cortical neurons (85). Although these reports achieve efficient photostimulation of neurons, the toxicity of QDs used in those studies raises concerns about their use in clinical applications. On the other hand, our group recently showed a biocompatible QD and its application for photostimulation of neurons (59). In this thesis, we show a systematic investigation of QD nanostructure and device structure to control the direction and amount of the stimulation. We present two different device structures: i) ITO/ZnO/QD (type I), ii) ITO/QD/ZnO (type II) in order to both depolarize and hyperpolarize neurons. With the optimized devices, we perform electrophysiology experiments and measure the photoelectrical response of cells by observing membrane potential changes via patch clamp setup in our lab.

4.2 Experimental work

4.2.1 Photoelectrode fabrication

We fabricated our InP-based photoelectrodes by spin coating method. A typical fabrication can be described as following:

Glass substrates covered with ITO were first cleaned with detergent solution, acetone, DI water and iso-propanol, consecutively, for 15 min each, and then treated with UV generated ozone for 15 min to increase the work function of ITO and further eliminate the residues on the ITO surface. Then, ZnO nanoparticles (synthesis details is provided in appendix) are spin coated at 2000 rpm from its 30 mg/ml solution on ITO. The ZnO coated substrates are baked at 90 C for 30 min. On top of ZnO, QD layer is formed by spin coating the QD solution (70 mg/ml) at 2000 rpm, and baking it at 100 C for 30 min. For type II devices, the procedure is the same except the coating sequence of ZnO and QD is reverse. Our fabrication area inside the fume hood is shown in Fig. 21.

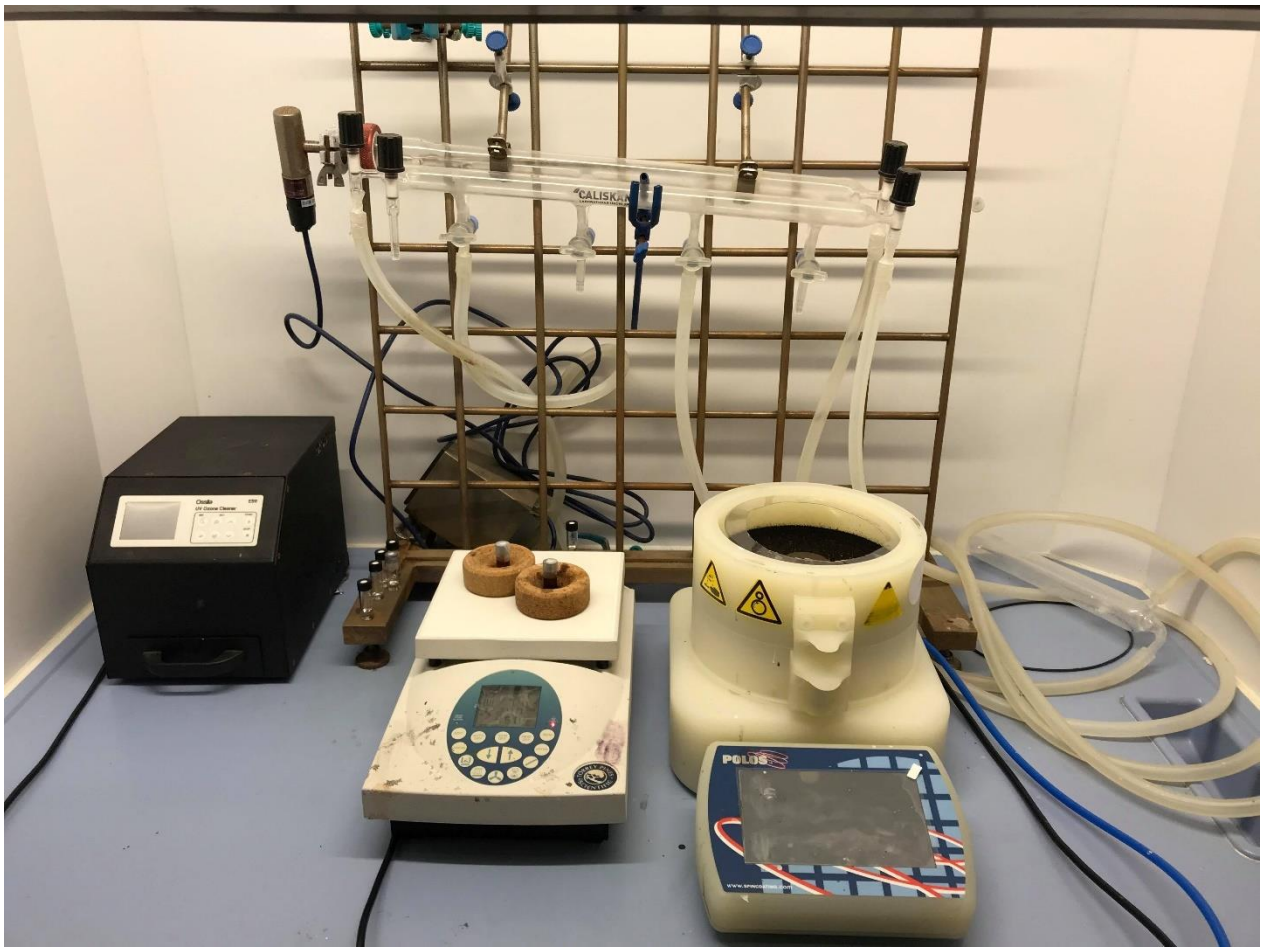

Figure 21: Photoelectrode fabrication instruments. From left to right: UV ozone cleaner, high sensitivity heater, and spin coater.

4.2.2 QD characterization

Toxicity of QDs synthesized from II-VI semiconductors (CdSe, HgTe, etc.) poses an obstacle for their use in biomedical applications. This obstacle led researchers to discover alternative non-toxic QDs. Synthesis of QDs from III-V semiconductors such as InP and AlSb offers potential for replacing QDs with toxic content (86). InP is most widely studied III-V QD which was previously used for QLEDs, biological imaging and labeling purposes (87-89). Therefore, InP QDs have well established and investigated synthesis procedures. For these reasons, we decided to use InP based QDs as the photoactive layer of our photoelectrodes.

It is known that covering core with a larger band gap shell passivates surface trap states and as a result increases quantum yield. Core/shell QDs are also more stable than core QDs. Considering the advantages of core/shell QDs, we synthesized both InP core and InP/ZnS core/shell QDs to compare their performances as photoactive layer. The QDs were synthesized using Nann's method (90) (details of synthesis are provided in the appendix). Fig. 22 shows absorption and photoluminescence emission plots of the synthesized InP and InP/ZnS QDs. One important observation from Fig. 22 is that InP/ZnS has higher absorbance than InP, which is an advantageous property for a photoactive layer.

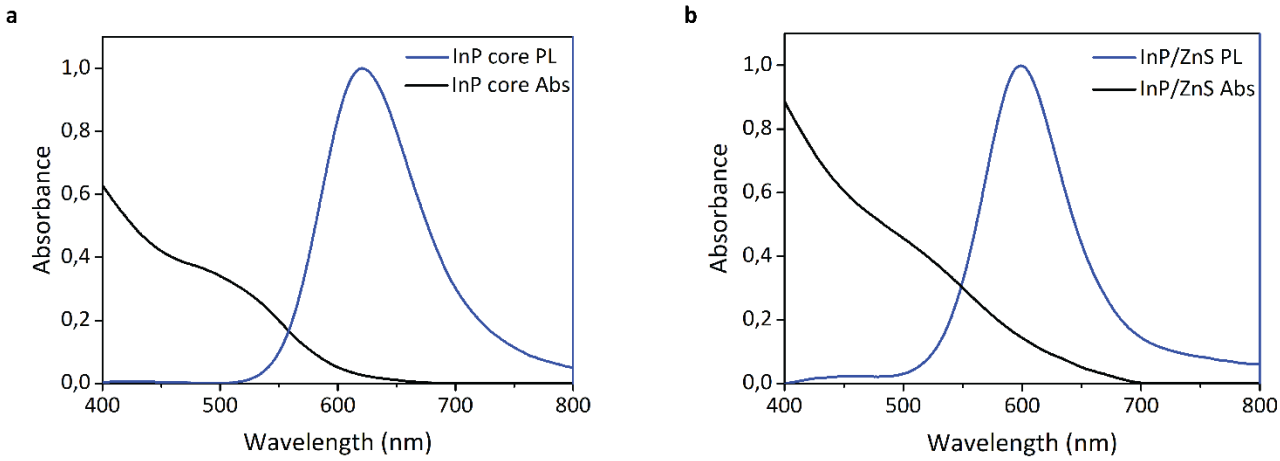

Figure 22: Absorption and photoluminescence emission plots of InP core and InP/ZnS core/shell QDs.

We also measured the PL QY of InP and InP/ZnS QDs using an integrating sphere. The QY of InP is 3%, while the QY of InP/ZnS is 15%. 5-fold increase in PL QY implies the successful passivation of surface trap states of InP core.

4.2.3 Photoelectrode design and experimental results

In order to have a control on the direction of neural stimulation, we need to obtain both cathodic and anodic photocurrent with our photoelectrodes. Anodic current will depolarize the neurons, while cathodic current will lead to hyperpolarization. To achieve this bidirectional photocurrent, we designed devices in two different structures: *i)* ITO/ZnO/QD (type I) *ii)* ITO/QD/ZnO (type II).

ZnO nanoparticles layer is used as an intermediate layer which blocks holes. The device structures and corresponding energy band diagrams are shown in Fig. 23. The working mechanism of type I and type II devices will be as following:

Illumination of photoelectrodes will create electron-hole pairs. According to the energy diagrams, electrons will migrate towards ITO in type I devices. Holes will be blocked by ZnO layer and accumulate on the surface, which will create anodic photocurrent. On the other hand, photogenerated holes cannot move to the surface in type II devices due to the deep valence band energy level of ZnO. This leads to electron accumulation on the surface, and as a result cathodic photocurrent for type-II devices.

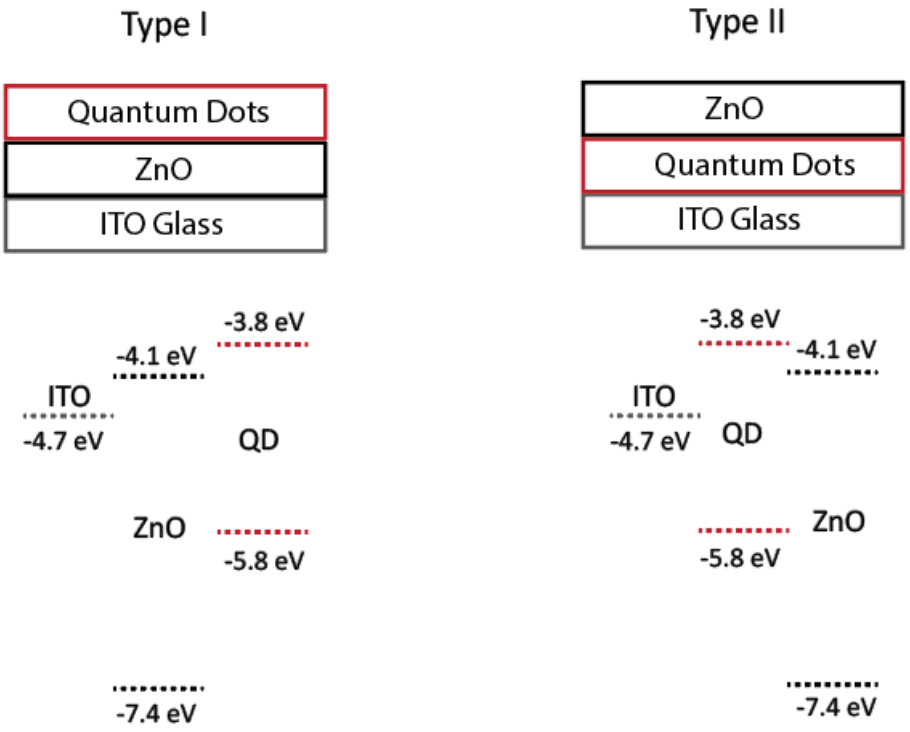

Figure 23: Two different device structures and corresponding energy band diagrams for having bidirectional stimulation.

After designing the electrodes, we measured their electrical response under illumination via a patch clamp system. Our patch clamp system is shown in Fig. 24.

Figure 24: Patch clamp setup in our lab. On the right, computer, patch clamp amplifier and microcontrollers for microscope and pipette holder can be seen. On the left, microscope, pipette holder, optical setup and sample holder is located on the optical table.

Schematic illustration of our measurement setup is shown in Fig. 25. We place our photoelectrodes in artificial cerebrospinal fluid (aCSF) to mimic the real-life scenario for neurons (Preparation of aCSF is provided in the appendix). Since we will perform electrophysiology experiments with micropipettes which have resistances of several megaohms, we measure photocurrents also with

micropipettes with a similar resistance to have consistent data with electrophysiology. Patch clamp setup measures the potential difference between Ag/AgCl electrode inside the pipette and ground electrode, and reports the corresponding photocurrent value. We measured the photocurrents of photoelectrodes under 1 mW/cm^2 illumination with 450 nm commercial blue LED.

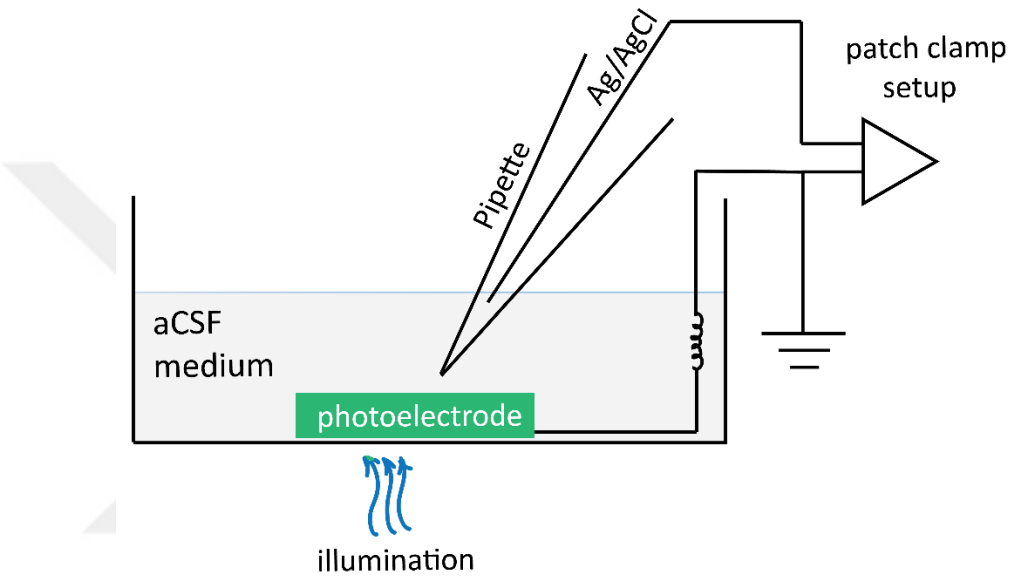

Figure 25: Schematic of measurement setup for characterization of photoelectrical response of photoelectrodes.

We expect anodic photocurrent from type I devices and cathodic photocurrent from type II devices. Fig X presents the photocurrent measurement of type I and type II devices under 1 mW/cm^2 illumination with 100 ms pulses. The resulting photocurrent directions agree with our expectation. Fig 26a shows the anodic photocurrent with type I devices, while Fig 26c shows the cathodic current for type II devices. We also measured photocurrent values for different durations of pulses (10, 100, 500, 1000 ms) which are shown in Fig 26b and Fig 26d. As the pulse duration gets longer, photocurrents increase and start to saturate after some point. Type II devices produce higher photocurrent compared to type I devices (maximum 4.35 nA for type II and 1.25 nA for type I).

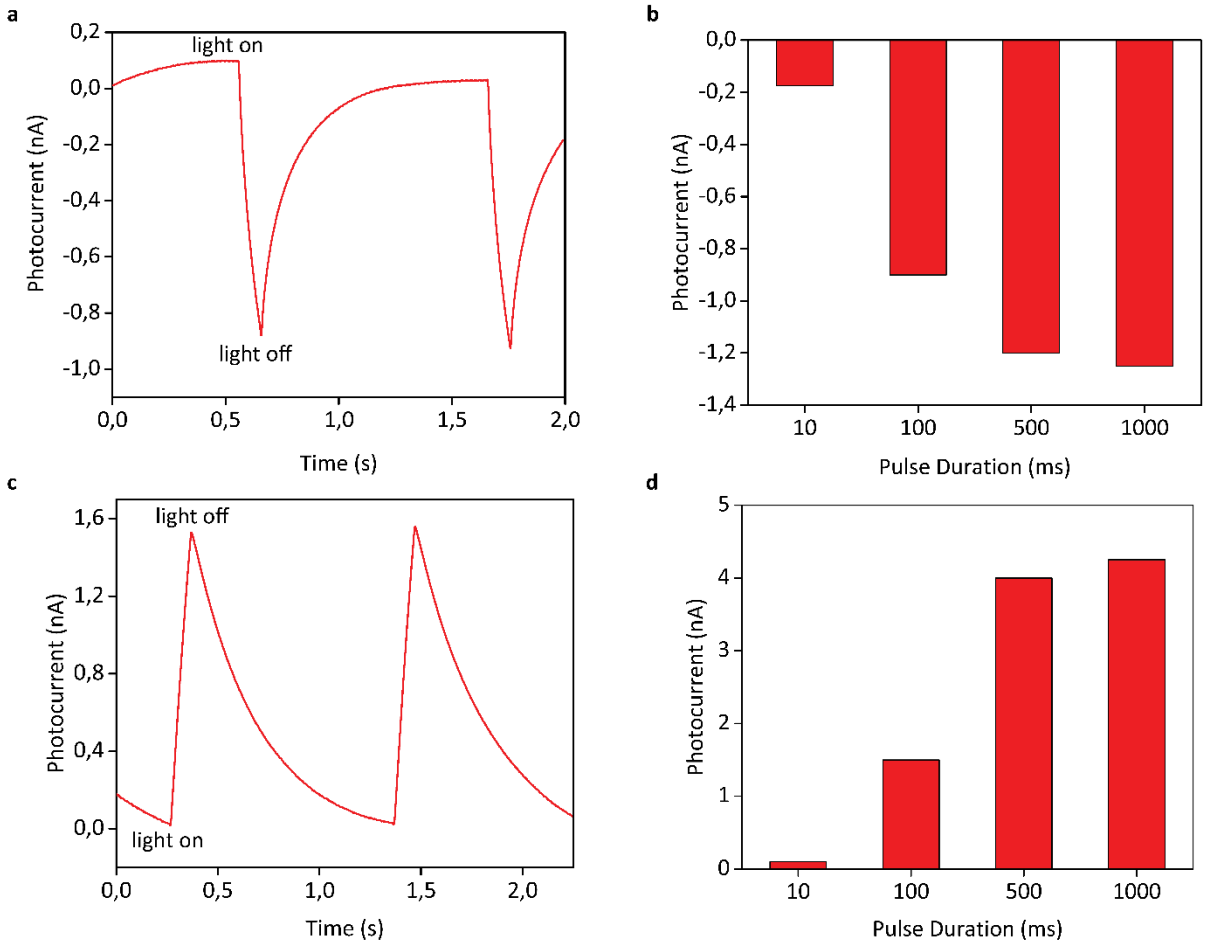

Figure 26: Photocurrent response of a) type I device under 100 ms pulse illumination, b) type I device for different durations of pulses, c) type II device under 100 ms pulse illumination, d) type II device for different durations of pulses.

Next, we compared the photoelectrical responses of photoelectrodes with InP and InP/ZnS photoactive layers. Devices that have InP/ZnS photoactive layer produce higher photocurrents than the devices with InP photoactive layer for both types of devices (Fig. 27). We think that the reason behind this is the decreased amount of defect states in InP/ZnS. Defect states serve as available states that can be occupied by electrons and holes. Thus, photogenerated electrons/holes can move into defect states, which would decrease the charge flow in the device, thus, decreases the photocurrent. Decreased amount of defect states can be deduced from the 5-fold enhancement in PL QY of InP/ZnS.

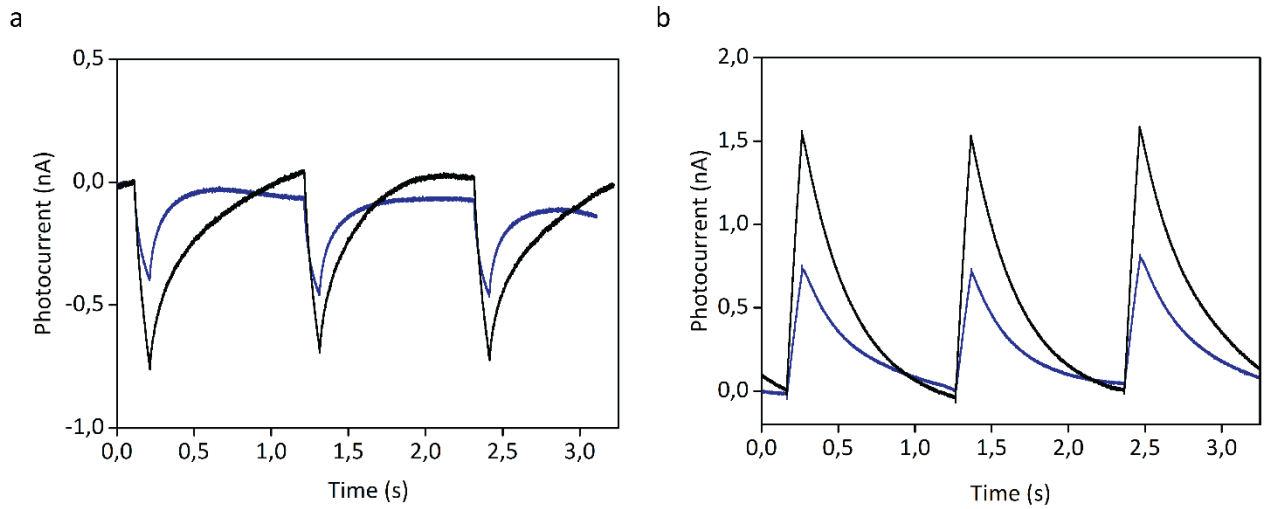

Figure 27: Photocurrents of a) type I devices with InP photoactive layer (blue), InP/ZnS photoactive layer (black), b) type II devices with InP photoactive layer, InP/ZnS photoactive layer (black).

Since type II photoelectrodes have higher photocurrent than type I devices, we performed the electrophysiology experiments with type II devices. Before that, we also optimized the thickness of the photoactive layer by measuring the photocurrents of devices with different photoactive layer thicknesses. We fabricated devices with 1, 2, 3, 4 and 5 times coated photoactive layers. As seen in Fig. 28, photocurrent first increases when we move from 1 times coated device to 2 times coated one, but then it decreases as the photoactive layer gets further thicker. Thus, there is an optimum thickness that maximizes the photocurrent of the devices. We explain the reason for the behavior of photocurrent-thickness function as following:

When the photoactive layer is too thin, the absorption will be low and most of the incident light will transmit through the photoactive layer. On the other hand, when the photoactive layer is too thick, the energy of photogenerated electrons and holes will not be enough for them to cross photoactive layer and migrate to another layer.

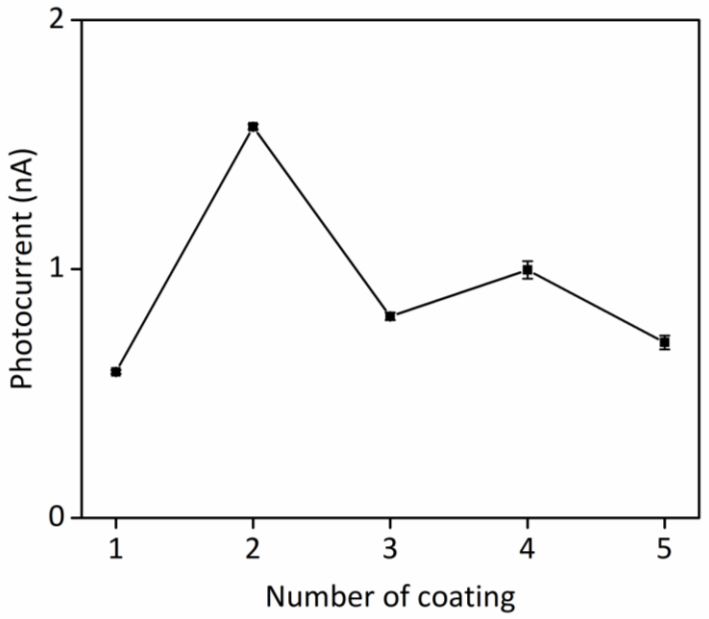

Figure 28: Photocurrent of type II devices as a function of number of coating of photoactive layer for type II photoelectrodes.

Finally, we moved on to the electrophysiology experiments with human neuroblastoma cell line, SH-SY5Y neurons. SH-SY5Y cells were grown on top of the photoelectrodes we fabricated. In aCSF medium, we measured the membrane potential variations of SH-SY5Y cells under illumination via patch clamp setup. Schematic of our experiment setup is shown in Fig. 29a. After we form giga-seal with the cell membrane and switch to the whole-cell mode, we measured the current-voltage characteristic of the cells in voltage clamp mode (Fig. 29b). IV plot shows the membrane voltage value as -50 mV, which agrees with the previous studies with SH-SY5Y cells (91, 92). Next, we measured the membrane voltage variations of cells under illumination in current clamp mode. Since the photoelectrodes used in these experiments are type II electrodes which have cathodic photocurrent, we expect the cell membrane to hyperpolarize. This is what we observed experimentally in Fig. 29c, which shows the hyperpolarization of cell membrane under 100 ms pulses. The hyperpolarization amount is around 3.5 mV. We can hyperpolarize the cells more by increasing the pulse duration or similarly hyperpolarize less by decreasing the pulse duration. The corresponding hyperpolarization amounts to the pulse durations is shown in Fig. 29d.

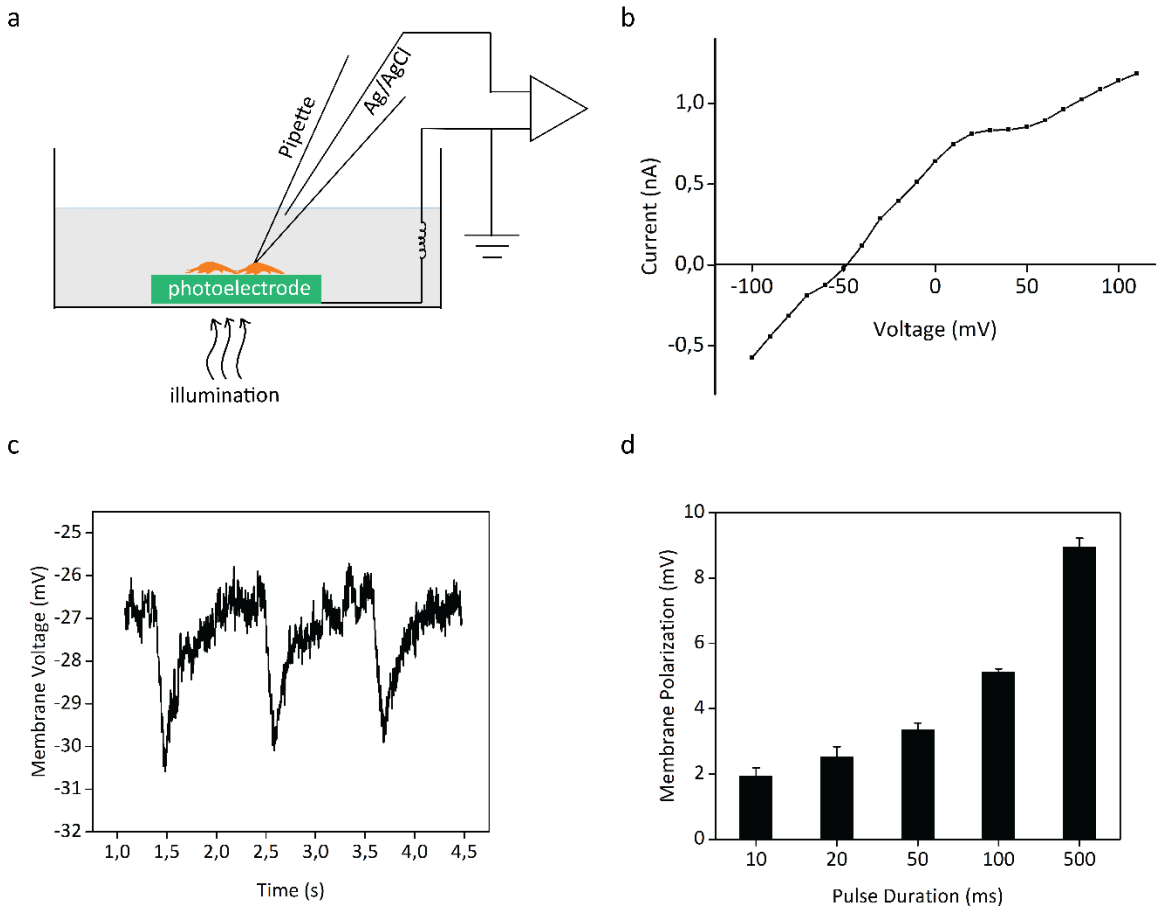

Figure 29: Electrophysiology experiment with SH-SY5Y neurons. a) Schematic of experiment setup, b) IV plot of cells in voltage clamp mode, c) membrane potential variations of SH-SY5Y cells under illumination measured in current clamp mode, d) membrane polarization amplitudes for different pulse durations.

4.3 Conclusion

QDs are promising materials for photoactive layers, and photoactive surfaces have potential applications in optical stimulation of neurons. Using photoactive layers that do not have toxic content reassures the concerns about their biological applications. We showed that InP based QDs can be used as photoactive layers for the optical stimulation for neurons. We demonstrated that proper band alignment engineering can lead to bidirectional current, which can be used to depolarize or hyperpolarize the neurons.

CHAPTER 5 Discussion & Conclusion

With the rapidly increasing demand to optoelectronic devices, interest in alternative materials with superior optoelectronic properties also increases. QDs are considered among such materials, which have a potential to replace silicon and organic semiconductors in certain applications in the near future. Apart from their costly production, toxicity of QDs is another major concern that hinders the commercialization of QD technology fully. Thus, researchers pay significant attention to explore QDs with minimum toxic content. To serve this purpose, we studied two different optoelectronic application of InP based QDs and showed that InP QDs can be alternative in multiple areas to their toxic counterparts.

The bullet points of this thesis can be listed as following:

1) First time demonstration of non-toxic type-II QD based LEDs (93)

The material we use as the active layer of our QLEDs, InP/ZnO QDs, is introduced to the literature by our group (29). Although type II QDs do not attract much attention for QLEDs, we showed that well performing QLEDs can be fabricated with InP based type II QDs (93).

- In terms of luminance, our QLEDs showed the second highest luminance (600 cd/m^2) among red InP based QLEDs as of the publication date of our article (52, 53).

- Low turn on voltage (2.8 V), and saturated color emission of our QLEDs are also favorable for their application in display technology.

- We showed the systematic investigation of minimizing solid state efficiency loss of QDs by maximizing the Stoke's shift via controlling the shell thickness of InP/ZnO QDs.

- We emphasized the importance of optimization of layer thicknesses on device efficiency.

2) First time illustration of proper photoelectrode design which can both stimulate and silence neurons via light.

Although researchers have put a lot of effort for producing effective neural stimulation electrodes, there is no simple procedure in the literature to design devices that can both stimulate and silence neurons. We showed that by proper band alignment engineering, InP QD based photoelectrodes

create bidirectional current which can be used for depolarization or hyperpolarization of neurons via light.

- After a recent report from our group (59), this study is another example of neural photostimulation with non-toxic InP-based QDs.

- We presented the characterization of core/shell nanostructure for more effective photoelectrical performance.

- Photocurrent depends on the thickness of photoactive layer. By fabrication of devices with different photoactive layer thickness, it is possible to control the amount of membrane potential change of neurons.

There can be many other applications of InP QDs, and our studies in this thesis can be considered as proof-of-concept demonstrations of such possible applications. QDs hold great promise for various optoelectronic applications, and continuous research on discovery of alternative materials, understanding the fundamentals and finding suitable applications of QDs can lead to many more scientific and technological advancements.

APPENDIX

Synthesis Procedures

InP core, InP/ZnO and InP/ZnS QDs were synthesized based on our previous reports (29, 65).

Indium Phosphide Core Synthesis (29)

Zinc undecylenate (0.3 mmol), 98 μL of OA, and 204 μL of OAM were mixed in 9 mL of ODE in a 100 mL three-neck round-bottom flask. The solution was heated to 100 °C, evacuated, and refilled with nitrogen repeatedly to provide an oxygen- and water-free reaction atmosphere. InCl3 (0.3 mmol) was then added to the solution in the glovebox. The flask was heated to 240 °C with strong agitation under nitrogen flow. At this temperature, 1.5 mL of phosphine stock solution (P(TMS)3−ODE 0.2 mmol mL^{-1}) was injected to the solution swiftly. The color of the solution became dark right after the injection. The dark solution was kept at 210 °C for 20 min and then cooled down to room temperature.

Preparation of 0.015 M Zinc Oxide Stock Solution for the Shelling Process (29)

Zn(acac)2 (0.1 mmol), 32 μL of OA, and 1 mL of OAM were mixed in 6 mL of ODE at 60 °C.

InP/ZnO Quantum Dot Synthesis (29)

The solution containing indium phosphide QDs was heated to 60 °C. Once the temperature was stable, 530 μL of the prepared zinc oxide stock solution was added to the indium phosphide solution. Then, the solution was heated up to 280 °C and stirred for 20 min.

Indium Phosphide Quantum Dots with Multiple Shelling of Zinc Oxide (29)

(For InP/1ZnO) and 2120 μL (For InP/2ZnO) of the prepared zinc oxide stock solution which contains 0.1 mmol Zn(acac)2, 32 μL of oleic acid, 1 mL of oleylamine and 6 ml 1-Octadecene was added to the indium phosphide core solution at 60 C. Then, solution was heated up to 280 °C and stirred for 20 min under N2 atmosphere. The final QDs was purified by centrifugation at 6000 rpm for 15 min then dispersed in toluene and kept in 5 C.

Transmission Electron Microscopy (TEM) Images and Size Distribution of InP/ZnO (59)

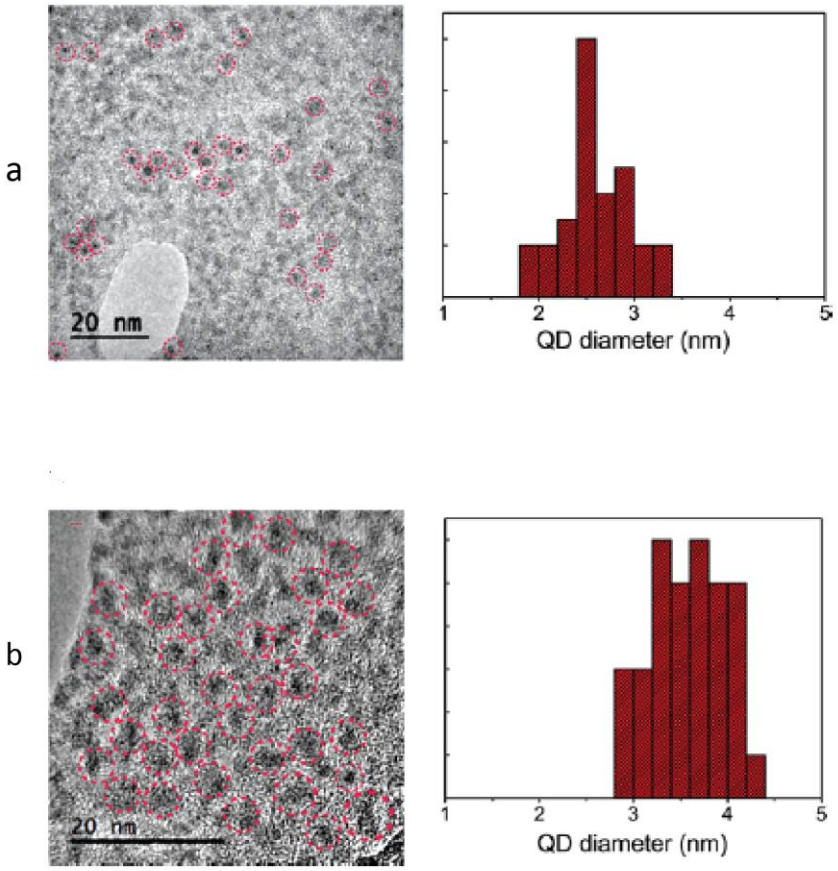

Figure 30: High resolution transmission electron microscopy images (HR-TEM) and size distribution plots of a) InP core, b) InP/ZnO core shell QDs (60).

Synthesis of InP/ZnS colloidal QDs

Hexadecylamine (HDA) (99%), zinc undecylenate (99%), 1-Octadecene (ODE) (90%), indium chloride (InCl3) (99%), Tris(trimethylsilyl) phosphine (P(TMS)3) (95%) and zinc diethyldithiocarbamate (97%) were purchased from sigma-aldrich. ODE was purified at 100 °C by making evacuation and refill with nitrogen for 1h. Nann`s method was used to synthesize InP/ZnS QDs (90) . Firstly, 96 mgr HDA and 86 mgr zinc undecylenate were mixed in a three-neck flask with 6 ml ODE. The solution was heated to 100 ºC, evacuated and refilled with nitrogen for two times to provide oxygen and water-free reaction atmosphere. Then, 44 mgr indium chloride was added to the solution in the glove-box. Again, the solution was heated to 100 ºC, evacuated and refill with nitrogen. The flask was heated to 260 ºC (10 °C/min) with strong agitation under nitrogen

flow. At this temperature, 1 ml of P(TMS)3 stock solution (0.2 mM) was injected to the solution very swiftly. The color of the solution was changed suddenly after injection. The solution was kept at 220 ºC for 20 min and then cooled down to room temperature. For the ZnS shell, 54 mgr zinc S2 diethyldithiocarbamate and 2 ml ODE were added to the above InP solution at room temperature and heated up to 250 ºC and stirred for 20 min. The flask was cooled down to room temperature and half of the solution was taken and labeled as InP/ZnS.

Synthesis of ZnO Nanoparticles

ZnO nanoparticles were synthesized using a previously reported method (71). In a typical synthesis, 20 ml solution of tetramethylammonium hydroxide (TMAH) dissolved in ethanol (0.55 M) was dropwisely added (1 ml/min) to a 30 ml solution of zinc acetate dihydrate dissolved in dimethyl sulfoxide (DMSO) (0.5 M). The solution was stirred vigorously for 1h at room temperature. Afterwards, it was washed with toluene and re-dispersed in ethanol at a concentration of 30 mg/ml.

Instrumentation and characterization

UV/Visible absorption and photoluminescence spectra of QDs were performed with Edinburgh Instruments Spectrofluorometer FS5 which includes a 150 W Xenon lamp combined with an excitation monochromator. The excitation wavelength was 375 nm with a band pass filter that has 2 nm full width at half maximum (FWHM). Emission detector was a single photon counting photomultiplier tube (R928P) with 2 nm spectral width. Absolute fluorescence quantum yield values were measured by placing the measurement module, which contains an integrating sphere with inner diameter of 150 mm, into FS5 system. Layer thicknesses are characterized using Dimension Icon Bruker AFM device. Current density-voltage-luminance (J-V-L) characteristics of QLEDs were carried out using a Keithley 2400 voltage-current source unit together with JETI Specbos 1211 Spectro-radiometer. Current efficiency was then calculated by multiplying the luminance values with the device area; and dividing it with the corresponding current values obtained from current-voltage (IV) data. External quantum efficiency (EQE) values were

calculated based on a recommended method in literature(94), using a calibrated silicon photodetector (Newport 818-UV) with a known responsivity. QLEDs were placed close to photodetector and the edges of the devices were covered with black tape to mask emerging photons from the edges of the substrates. EQE values were then inferred from the photocurrent of the detector. Electroluminescence (EL) spectrum and color coordinates of the devices were obtained using Labsphere integrating sphere. PL decays were taken by PicoQuant MicroTime 100 time-resolved confocal fluorescence microscope. The samples were excited by an 8 mW picosecond diode laser (λexc = 375 nm) pulsed at 60 MHz repetition rate to 40X objective lens. PL decays were fit by a two-exponential decay and the average life-time (τ_{avg}) was calculated from an amplitude weighted mean(95) (Details can be seen in Table S1). Ultraviolet photoelectron spectroscopy measurements were performed using Specs FlexMod system.

Tauc plots for InP core, InP/1ZnO and InP/2ZnO showing their band gaps

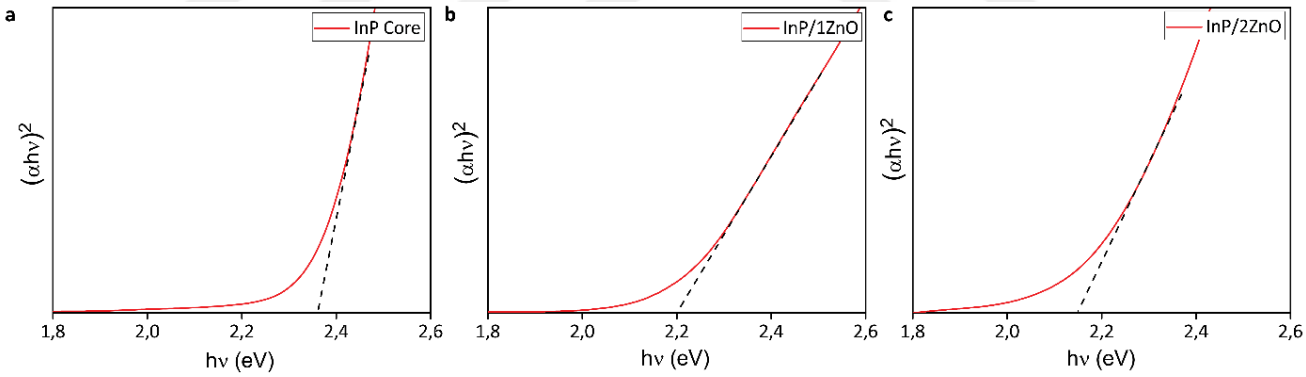

Figure 31: Tauc plot of a) InP core, b) InP/1ZnO, and c) InP/2ZnO QDs.

Photocurrent and electrophysiology

An EPC 800 patch clamp amplifier (HEKA Elektronik) is used for the electrophysiology and the photocurrent measurements. Pulled patch pipettes with 6–10 MΩ resistances are used to perform the whole neuron cells under a giga-Ohm seal. Extracellular medium [artificial cerebrospinal fluid (aCSF)] is prepared by mixing 10 mM of 4-(2-hydroxyethyl)-1-piperazineethanesulfonic acid (HEPES), 10 mM of glucose, 2 mM of CaCl2, 140 mM of NaCl, 1 mM of $MgCl_2$, 3 mM of KCl,

and NaOH into the distilled water at a pH of 7.4. Internal cellular medium is made by mixing 140 mM of KCl, 2 mM of $MgCl_2$, 10 mM of HEPES, 10 mM of ethylene glycol-bis(β-aminoethyl ether)-N,N,N',N'-tetraacetic acid (EGTA), 2 mM of Mg-ATP, and KOH at a pH of 7.2, and is used to fill the patch pipettes. An Olympus T2 upright microscope and a digital camera are used in the electrophysiology set up to monitor the cells.

BIBLIOGRAPHY

1. Goodship V, Stevels A, & Huisman J (2019) *Waste electrical and electronic equipment (WEEE) handbook* (Woodhead Publishing).
2. Baldé CP, Forti V, Gray V, Kuehr R, & Stegmann P (2017) *The global e-waste monitor 2017: Quantities, flows and resources* (United Nations University, International Telecommunication Union, and …).
3. Zhang K, Schnoor JL, & Zeng EY (2012) E-waste recycling: where does it go from here? (ACS Publications).
4. Chen A, Dietrich KN, Huo X, & Ho SM (2011) Developmental neurotoxicants in e-waste: an emerging health concern. *Environ Health Perspect* 119(4):431-438.
5. Ekimov AI, Efros AL, & Onushchenko AA (1985) Quantum size effect in semiconductor microcrystals. *Solid State Communications* 56(11):921-924.
6. Brus LE (1984) Electron–electron and electron-hole interactions in small semiconductor crystallites: The size dependence of the lowest excited electronic state. *The Journal of chemical physics* 80(9):4403-4409.
7. Yamazaki K*, et al.* (2000) Long term pulmonary toxicity of indium arsenide and indium phosphide instilled intratracheally in hamsters. *Journal of Occupational Health* 42(4):169-178.
8. Bharali DJ, Lucey DW, Jayakumar H, Pudavar HE, & Prasad PN (2005) Folate-receptor-mediated delivery of InP quantum dots for bioimaging using confocal and two-photon microscopy. *Journal of the American Chemical Society* 127(32):11364-11371.
9. Panfil YE, Oded M, & Banin U (2018) Colloidal Quantum Nanostructures: Emerging Materials for Display Applications. *Angew Chem Int Ed Engl* 57(16):4274-4295.
10. Brus L (1986) Electronic wave functions in semiconductor clusters: experiment and theory. *The Journal of Physical Chemistry* 90(12):2555-2560.
11. Eustis S & El-Sayed MA (2006) Why gold nanoparticles are more precious than pretty gold: noble metal surface plasmon resonance and its enhancement of the radiative and nonradiative properties of nanocrystals of different shapes. *Chemical society reviews* 35(3):209-217.
12. Soloviev V, Eichhöfer A, Fenske D, & Banin U (2000) Molecular limit of a bulk semiconductor: size dependence of the “band gap” in CdSe cluster molecules. *Journal of the American Chemical Society* 122(11):2673-2674.
13. Dabbousi BO*, et al.* (1997) (CdSe) ZnS core− shell quantum dots: synthesis and characterization of a size series of highly luminescent nanocrystallites. *The Journal of Physical Chemistry B* 101(46):9463-9475.
14. Chen O*, et al.* (2013) Compact high-quality CdSe–CdS core–shell nanocrystals with narrow emission linewidths and suppressed blinking. *Nature materials* 12(5):445.
15. Hanifi DA*, et al.* (2019) Redefining near-unity luminescence in quantum dots with photothermal threshold quantum yield. *Science* 363(6432):1199-1202.
16. Kagan CR, Lifshitz E, Sargent EH, & Talapin DV (2016) Building devices from colloidal quantum dots. *Science* 353(6302).
17. Hens Z & Moreels I (2012) Light absorption by colloidal semiconductor quantum dots. *Journal of Materials Chemistry* 22(21):10406-10415.
18. de Graaf G & Wolffenbuttel RF (2004) Illumination source identification using a CMOS optical microsystem. *IEEE Transactions on Instrumentation and Measurement* 53(2):238-242.
19. Talapin DV*, et al.* (2004) CdSe/CdS/ZnS and CdSe/ZnSe/ZnS Core− Shell− Shell Nanocrystals. *The Journal of Physical Chemistry B* 108(49):18826-18831.

20. Zhang J, Tang Y, Lee K, & Ouyang M (2010) Nonepitaxial growth of hybrid core-shell nanostructures with large lattice mismatches. *Science* 327(5973):1634-1638.
21. Kumar BG*, et al.* (2018) Structural control of InP/ZnS core/shell quantum dots enables high-quality white LEDs. *Nanotechnology* 29(34):345605.
22. Shirasaki Y, Supran GJ, Bawendi MG, & Bulović V (2013) Emergence of colloidal quantum-dot light-emitting technologies. *Nature photonics* 7(1):13.
23. van Sark WG, Frederix PL, Bol AA, Gerritsen HC, & Meijerink A (2002) Blueing, bleaching, and blinking of single CdSe/ZnS quantum dots. *ChemPhysChem* 3(10):871-879.
24. Mastria R & Rizzo A (2016) Mastering heterostructured colloidal nanocrystal properties for light-emitting diodes and solar cells. *Journal of Materials Chemistry C* 4(27):6430-6446.
25. Colvin V, Schlamp M, & Alivisatos AP (1994) Light-emitting diodes made from cadmium selenide nanocrystals and a semiconducting polymer. *Nature* 370(6488):354.
26. Schubert EF (2006) *Light-Emitting Diodes (Second Edition, 2006)* (E. Fred Schubert).
27. Wood V & Bulović V (2010) Colloidal quantum dot light-emitting devices. *Nano reviews* 1(1):5202.
28. Shen H*, et al.* (2019) Visible quantum dot light-emitting diodes with simultaneous high brightness and efficiency. *Nature Photonics* 13(3):192-197.
29. Sadeghi S*, et al.* (2018) Stokes-Shift-Engineered Indium Phosphide Quantum Dots for Efficient Luminescent Solar Concentrators. *ACS Appl Mater Interfaces* 10(15):12975-12982.
30. Sun Y & Forrest SR (2008) Enhanced light out-coupling of organic light-emitting devices using embedded low-index grids. *Nature Photonics* 2:483.
31. Möller S & Forrest S (2002) Improved light out-coupling in organic light emitting diodes employing ordered microlens arrays. *Journal of Applied Physics* 91(5):3324-3327.
32. Tsutsui T, Yahiro M, Yokogawa H, Kawano K, & Yokoyama M (2001) Doubling coupling-out efficiency in organic light-emitting devices using a thin silica aerogel layer. *Advanced Materials* 13(15):1149-1152.
33. Brütting W, Frischeisen J, Schmidt TD, Scholz BJ, & Mayr C (2013) Device efficiency of organic light-emitting diodes: Progress by improved light outcoupling. *physica status solidi (a)* 210(1):44-65.
34. Reineke S*, et al.* (2009) White organic light-emitting diodes with fluorescent tube efficiency. *Nature* 459(7244):234.
35. Anonymous (2006) Light's labour's lost : policies for energy-efficient lighting. eds Waide P & Tanishima S (OECD :, Paris :).
36. Colvin VL, Schlamp MC, & Alivisatos AP (1994) Light-emitting diodes made from cadmium selenide nanocrystals and a semiconducting polymer. *Nature* 370:354.
37. Coe S, Woo W-K, Bawendi M, & Bulović V (2002) Electroluminescence from single monolayers of nanocrystals in molecular organic devices. *Nature* 420:800.
38. Shen H*, et al.* (2015) High-efficiency, low turn-on voltage blue-violet quantum-dot-based light-emitting diodes. *Nano Lett* 15(2):1211-1216.
39. Caruge JM, Halpert JE, Wood V, Bulović V, & Bawendi MG (2008) Colloidal quantum-dot light-emitting diodes with metal-oxide charge transport layers. *Nature Photonics* 2:247.
40. Zhang Y*, et al.* (2011) Employing heavy metal-free colloidal quantum dots in solution-processed white light-emitting diodes. *Nano Lett* 11(2):329-332.
41. Nizamoglu S*, et al.* (2008) Dual-color emitting quantum-dot-quantum-well CdSe-ZnS heteronanocrystals hybridized on InGaN⁄GaN light emitting diodes for high-quality white light generation. *Applied Physics Letters* 92(11).
42. Alivisatos AP (1996) Semiconductor Clusters, Nanocrystals, and Quantum Dots. *Science* 271:933-937.

43. Kim S*, et al.* (2012) Highly luminescent InP/GaP/ZnS nanocrystals and their application to white light-emitting diodes. *J Am Chem Soc* 134(8):3804-3809.
44. Qian G*, et al.* (2014) Saturated and Multi-Colored Electroluminescence from Quantum Dots Based Light Emitting Electrochemical Cells. *Advanced Functional Materials* 24(28):4484-4490.
45. Sadeghi S*, et al.* (2018) Quantum dot white LEDs with high luminous efficiency. *Optica* 5(7).
46. Mashford BS*, et al.* (2013) High-efficiency quantum-dot light-emitting devices with enhanced charge injection. *Nature Photonics* 7(5):407-412.
47. Yang Y*, et al.* (2015) High-efficiency light-emitting devices based on quantum dots with tailored nanostructures. *Nature Photonics* 9(4):259-266.
48. Dai X*, et al.* (2014) Solution-processed, high-performance light-emitting diodes based on quantum dots. *Nature* 515:96.
49. Shirasaki Y, Supran GJ, Bawendi MG, & Bulović V (2013) Emergence of colloidal quantum-dot light-emitting technologies. *Nature Photonics* 7(1):13-23.
50. Wang HC*, et al.* (2017) Cadmium-Free InP/ZnSeS/ZnS Heterostructure-Based Quantum Dot Light-Emitting Diodes with a ZnMgO Electron Transport Layer and a Brightness of Over 10 000 cd m(-2). *Small* 13(13).
51. Lim J*, et al.* (2013) Highly Efficient Cadmium-Free Quantum Dot Light-Emitting Diodes Enabled by the Direct Formation of Excitons within InP@ZnSeS Quantum Dots. *ACS Nano* 7(10):9019-9026.
52. Jo JH*, et al.* (2016) High-efficiency red electroluminescent device based on multishelled InP quantum dots. *Opt Lett* 41(17):3984-3987.
53. Kim HY*, et al.* (2016) Transparent InP Quantum Dot Light-Emitting Diodes with ZrO2Electron Transport Layer and Indium Zinc Oxide Top Electrode. *Advanced Functional Materials* 26(20):3454-3461.
54. Lin Q*, et al.* (2016) High-efficiency deep-red quantum-dot light-emitting diodes with type-II CdSe/CdTe core/shell quantum dots as emissive layers. *Journal of Materials Chemistry C* 4(30):7223-7229.
55. Jin X*, et al.* (2018) Bright alloy type-II quantum dots and their application to light-emitting diodes. *J Colloid Interface Sci* 510:376-383.
56. Meinardi F*, et al.* (2014) Large-area luminescent solar concentrators based on 'Stokes-shift-engineered'nanocrystals in a mass-polymerized PMMA matrix. *Nature Photonics* 8(5):392.
57. Meinardi F*, et al.* (2014) Large-area luminescent solar concentrators based on 'Stokes-shift-engineered' nanocrystals in a mass-polymerized PMMA matrix. *Nature Photonics* 8:392.
58. Coropceanu I & Bawendi MG (2014) Core/Shell Quantum Dot Based Luminescent Solar Concentrators with Reduced Reabsorption and Enhanced Efficiency. *Nano Letters* 14(7):4097-4101.
59. Bahmani Jalali H*, et al.* (2018) Effective Neural Photostimulation Using Indium-Based Type-II Quantum Dots. *ACS Nano* 12(8):8104-8114.
60. Brovelli S*, et al.* (2011) Nano-engineered electron-hole exchange interaction controls exciton dynamics in core-shell semiconductor nanocrystals. *Nat Commun* 2:280.
61. Garcia-Santamaria F*, et al.* (2011) Breakdown of volume scaling in Auger recombination in CdSe/CdS heteronanocrystals: the role of the core-shell interface. *Nano Lett* 11(2):687-693.
62. Pal BN*, et al.* (2012) 'Giant' CdSe/CdS core/shell nanocrystal quantum dots as efficient electroluminescent materials: strong influence of shell thickness on light-emitting diode performance. *Nano Lett* 12(1):331-336.
63. Bischof TS, Caram JR, Beyler AP, & Bawendi MG (2016) Extracting the average single-molecule biexciton photoluminescence lifetime from a solution of chromophores. *Opt. Lett.* 41(20):4823-4826.

64. Purcell-Milton F*, et al.* (2017) Impact of Shell Thickness on Photoluminescence and Optical Activity in Chiral CdSe/CdS Core/Shell Quantum Dots. *ACS Nano* 11(9):9207-9214.
65. Bahmani Jalali H, Melikov R, Sadeghi S, & Nizamoglu S (2018) Excitonic Energy Transfer within InP/ZnS Quantum Dot Langmuir-Blodgett Assemblies. *J Phys Chem C Nanomater Interfaces* 122(22):11616-11622.
66. Talapin DV, Rogach AL, Kornowski A, Haase M, & Weller H (2001) Highly Luminescent Monodisperse CdSe and CdSe/ZnS Nanocrystals Synthesized in a Hexadecylamine−Trioctylphosphine Oxide−Trioctylphospine Mixture. *Nano Letters* 1(4):207-211.
67. Peng X, Schlamp MC, Kadavanich AV, & Alivisatos AP (1997) Epitaxial growth of highly luminescent CdSe/CdS core/shell nanocrystals with photostability and electronic accessibility. *Journal of the American Chemical Society* 119(30):7019-7029.
68. Wood V & Bulović V (2010) Colloidal quantum dot light-emitting devices. *Nano Reviews* 1:10.3402/nano.v3401i3400.5202.
69. Park N-G, Grätzel M, & Miyasaka T (2016) Organic-inorganic halide perovskite photovoltaics : from fundamentals to device architectures.
70. Kim HH*, et al.* (2015) Inverted Quantum Dot Light Emitting Diodes using Polyethylenimine ethoxylated modified ZnO. *Scientific Reports* 5:8968.
71. Qian L, Zheng Y, Xue J, & Holloway PH (2011) Stable and efficient quantum-dot light-emitting diodes based on solution-processed multilayer structures. *Nature Photonics* 5(9):543-548.
72. Sun JW*, et al.* (2014) A fluorescent organic light-emitting diode with 30% external quantum efficiency. *Adv Mater* 26(32):5684-5688.
73. Sun Q*, et al.* (2007) Bright, multicoloured light-emitting diodes based on quantum dots. *Nature Photonics* 1(12):717-722.
74. Greenham NC, Friend RH, & Bradley DDC (1994) Angular Dependence of the Emission from a Conjugated Polymer Light-Emitting Diode: Implications for efficiency calculations. *Advanced Materials* 6(6):491-494.
75. Lu MH & Sturm JC (2002) Optimization of external coupling and light emission in organic light-emitting devices: modeling and experiment. *Journal of Applied Physics* 91(2):595-604.
76. Fu H & Zunger A (1997) InP quantum dots: Electronic structure, surface effects, and the redshifted emission. *Physical Review B* 56(3):1496-1508.
77. Efros AL*, et al.* (1996) Band-edge exciton in quantum dots of semiconductors with a degenerate valence band: Dark and bright exciton states. *Physical Review B* 54(7):4843-4856.
78. Konstantatos G, Huang C, Levina L, Lu Z, & Sargent EH (2005) Efficient Infrared Electroluminescent Devices Using Solution-Processed Colloidal Quantum Dots. *Advanced Functional Materials* 15(11):1865-1869.
79. Adachi C, Baldo MA, Thompson ME, & Forrest SR (2001) Nearly 100% internal phosphorescence efficiency in an organic light-emitting device. *Journal of Applied Physics* 90(10):5048-5051.
80. Cogan SF (2008) Neural stimulation and recording electrodes. *Annu Rev Biomed Eng* 10:275-309.
81. Ghezzi D*, et al.* (2013) A polymer optoelectronic interface restores light sensitivity in blind rat retinas. *Nat Photonics* 7(5):400-406.
82. Jiang Y*, et al.* (2018) Rational design of silicon structures for optically controlled multiscale biointerfaces. *Nat Biomed Eng* 2(7):508-521.
83. Bareket-Keren L & Hanein Y (2014) Novel interfaces for light directed neuronal stimulation: advances and challenges. *International journal of nanomedicine* 9(Suppl 1):65.
84. Pappas TC*, et al.* (2007) Nanoscale engineering of a cellular interface with semiconductor nanoparticle films for photoelectric stimulation of neurons. *Nano letters* 7(2):513-519.
85. Lugo K, Miao X, Rieke F, & Lin LY (2012) Remote switching of cellular activity and cell signaling using light in conjunction with quantum dots. *Biomedical optics express* 3(3):447-454.

86. Bahmani Jalali H*, et al.* (2019) Colloidal Aluminum Antimonide Quantum Dots. *Chemistry of Materials*.
87. Ellis MA, Grandinetti G, & Fichter KM (2016) Synthesis of Cd-free InP/ZnS quantum dots suitable for biomedical applications. *JoVE (Journal of Visualized Experiments)* (108):e53684.
88. Lim J*, et al.* (2013) Highly efficient cadmium-free quantum dot light-emitting diodes enabled by the direct formation of excitons within InP@ ZnSeS quantum dots. *ACS nano* 7(10):9019-9026.
89. Yong K-T*, et al.* (2009) Imaging pancreatic cancer using bioconjugated InP quantum dots. *ACS nano* 3(3):502-510.
90. Xu S, Ziegler J, & Nann T (2008) Rapid synthesis of highly luminescent InP and InP/ZnS nanocrystals. *Journal of Materials Chemistry* 18(23):2653-2656.
91. Srivastava SB*, et al.* (2019) Band Alignment Engineers Faradaic and Capacitive Photostimulation of Neurons Without Surface Modification. *Physical Review Applied* 11(4):044012.
92. Santillo S, Moriello AS, & Di Maio V (2014) Electrophysiological variability in the SH-SY5Y cellular line. *Gen. Physiol. Biophys* 33:121-129.
93. Karatum O*, et al.* (2019) Light-Emitting Devices Based on Type-II InP/ZnO Quantum Dots. *ACS Photonics* 6(4):939-946.
94. Forrest SR, Bradley DDC, & Thompson ME (2003) Measuring the Efficiency of Organic Light-Emitting Devices. *Advanced Materials* 15(13):1043-1048.
95. Bahmani Jalali H, Melikov R, Sadeghi S, & Nizamoğlu S (2018) Excitonic Energy Transfer within InP/ZnS Quantum Dot Langmuir− Blodgett Assemblies. *The Journal of Physical Chemistry C*.